

A Study on Fault-Type and Site-Effect (V_{S30}) Parameters in the Attenuation Relationships of Peak Ground Acceleration and Peak Ground Velocity in Ilan, Taiwan

by Kun-Sung Liu, Yi-Ben Tsai, and Po-Shen Lin

Abstract The purpose of this study is to derive attenuation relationships of the peak ground acceleration (PGA) and peak ground velocity (PGV) in Ilan, Taiwan, including factors of fault type and site effect. A total of 2852 accelerograms recorded from 92 shallow earthquakes with M_w magnitude ranging from 4.0 to 7.7 are used to develop the regional attenuation relationships. Two models are used: Model 1 uses records from 65 strong-motion sites. The results will be especially useful for the Central Weather Bureau (CWB) early warning system to quickly assess and report the PGA and PGV maps for effective emergency-response operations. Model 2 uses records from the 46 strong-motion sites with available V_{S30} to incorporate a site-effect term, aiming to reduce the standard deviation of the predicted ground motion for engineering applications. First, the results show that the fault-type amplification factor decreases faster with increasing magnitude for the strike-slip fault type than the reverse or normal fault types. In addition, from the intraevent residuals as function of distance of horizontal PGA for reverse earthquakes, we found clusters of higher PGA values at a distance of 110–130 km from events in southwestern areas. This was probably due to Moho reflection along paths crossing the Central Mountain Range. Second, the PGV intraevent residual is more closely correlated with V_{S30} than that of the PGA because the latter is not a simple function of V_{S30} . Finally, by comparing the standard deviations of the total residuals between the observed and predicted values before and after incorporating the fault-type and site-effect (V_{S30}) terms, the change of standard deviation for PGA is 2.3%. In contrast, the PGV standard deviation is significantly decreased by about 11.6%. Evidently, the Model 2 attenuation relationships, especially for PGV, would be better suited for engineering applications.

Introduction

Ilan, our study area, lies in northeastern Taiwan. It neighbors New Taipei City by the Xueshan Mountain Range to the northwest. Since completion of the Taipei–Ilan freeway, the driving time to the Taipei metropolitan area has been significantly reduced. As a result, the population in the Ilan area is expected to increase rapidly. In the coming years, Ilan may see commencement of many major construction projects. Furthermore, the national government plans to establish the Ilan Science Park to promote the economy as well as to balance regional development. In order to ensure sufficient seismic safety of new constructions in the Ilan area, we have carried out this in-depth study of ground-motion characteristics to facilitate realistic seismic-hazard analyses.

Studies of ground-motion characteristics in the Ilan area require development of appropriate ground-motion attenuation relationships, or ground-motion prediction equations. These attenuation relationships will provide an efficient means

for predicting the level of ground shaking and its associated uncertainty at any given site or location in seismic-hazard analyses (Bolt and Abrahamson, 2004). An attenuation relationship is a mathematically based expression that relates a specific strong-motion parameter to relevant seismological parameters of an earthquake. These seismological parameters quantitatively characterize an earthquake source size and type, the wave-propagation path between the source and the site, and the soil and geological profile beneath the site (Campbell, 2004).

For development of ground-motion attenuation relationships, past developers have systematically evaluated a list of predictor parameters to account for the earthquake effects. Two of the most significant parameters found by all developers are related to the fault type and the average shear-wave velocity in the upper 30 m of sediments, V_{S30} (Power *et al.*, 2008). First, the fault-type parameter is used to distinguish

the effects of different source types. The ground motions generated by strike-slip, thrust, or normal-faulting earthquakes differ systematically. Given the same earthquake magnitude, distance to the site, and site condition, the ground motions from thrust earthquakes tend to be larger than those from strike-slip earthquakes by about 20%–30%. The ground motions from normal-faulting earthquakes tend to be smaller than those from strike-slip earthquakes by about 20% (Somerville and Abrahamson, 1995; Spudich *et al.*, 1996; Bolt and Abrahamson, 2004).

Second, past developers have used V_{S30} as the parameter for characterizing soil-stiffness effects on ground motions (Power *et al.*, 2008). Previously, most attenuation relationships used broad site categories, such as rock, stiff soil, and soft soil. Recently, there has been a move toward using quantitative site classifications based on the shear-wave velocity measured at a strong-motion site. The most commonly used parameter is the average shear-wave velocity over the top 30 m (V_{S30}) (Boore *et al.*, 1997; Bolt and Abrahamson, 2004).

Meanwhile, five groups of researchers developed new ground-motion models for application to the shallow crustal earthquakes in the western United States, as part of the Next Generation of Ground-Motion Attenuation Models (NGA) project. The project was coordinated by the Pacific Earthquake Engineering Research Center, in partnership with the U.S. Geological Survey and the Southern California Earthquake Center. The NGA-West project has resulted in a major improvement in the prediction of ground motions in the western United States. The five models all include a style-of-faulting factor. Four of the models include an additional parameter of V_{S30} to account for site effects (Abrahamson *et al.*, 2008). The NGA-West models provide much more robust and reliable estimates of ground motion than the previous generation of attenuation models developed in the 1990s and early 2000s (Boore and Atkinson, 2006, 2007; Campbell and Bozorgnia, 2006; Chiou and Youngs, 2006; Power *et al.*, 2008).

The Ilan area in northeastern Taiwan is affected by many earthquakes (Fig. 1). Accordingly, a large amount of strong-motion accelerograms have been recorded since the 1990s by the accelerographs installed in the Ilan area as part of the Taiwan Strong Motion Instrumentation Program (TSMIP) network. As the number of strong ground motion recordings increases, there has been a trend toward developing region-specific attenuation relationships, rather than just using the global average models developed for broad tectonic categories (Bolt and Abrahamson, 2004). Here we have a good opportunity to focus on the Ilan area to develop regional attenuation relationships and to systematically study the effects of style-of-faulting and site conditions.

In this study, we improve the attenuation relationships by incorporating a site-effect term, based on the average shear-wave velocity in the upper 30 m of sediments, V_{S30} , aiming to reduce the standard deviation of the predicted ground motion from large earthquakes. This approach emphasizes direct use of the recordings of strong ground motion

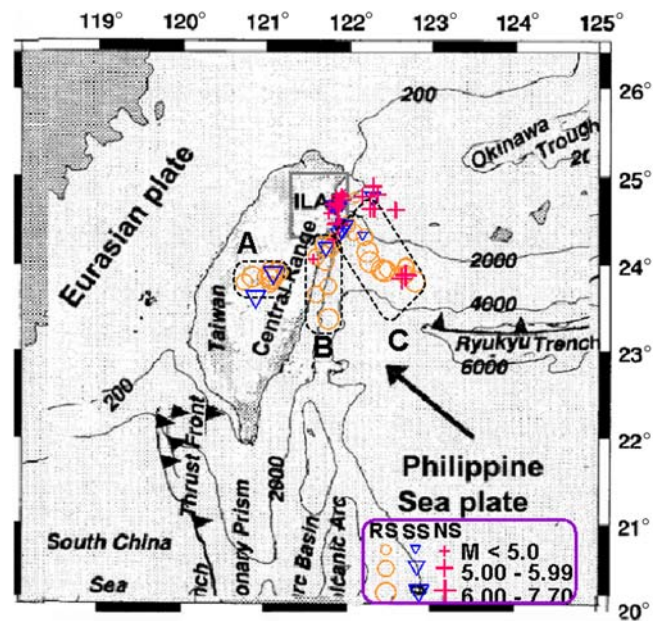


Figure 1. Seismotectonic setting of Taiwan and the surrounding area (adapted with permission from Rau and Wu, 1998). The epicenters of earthquakes used in this study are shown with symbols representing different fault types. The open circle, triangle, and cross represent the style of faulting for reverse, strike-slip, and normal fault, respectively. The three source areas of reverse earthquakes (i.e., areas A, B, and C) are also shown. The smaller rectangle shows our study area. The color version of this figure is available only in the electronic edition.

for estimation of seismic ground shaking for engineering purposes. Specifically, the purpose of this study is to derive attenuation relationships of peak ground acceleration (PGA) and peak ground velocity (PGV) in the Ilan area, and to analyze the effects of the style of faulting and site condition on these strong ground motion parameters. Hopefully, the results of this study can provide information for more realistic seismic-hazard analyses of critical facilities in this area.

The Data

Regional Setting

The study area, Ilan, constitutes an area of 2167 km². It has a triangular shape with a north–south side coincident with the northeastern coast of Taiwan and faces the Okinawa Trough toward the east. The two other sides are fringed, respectively, by the Xueshan Mountain Range in the northwest and the Central Mountain Range in the southwest, composed mainly of Miocene to Paleogene slates. The Lanyang River flows northeastward from the mountains into the Lanyang Plain. The area's landscape slopes downward from west to east, successively forming distinctive zones of mountains, valleys, alluvial plains, low wetlands, swamps, sand dunes, and beaches.

Tectonically, the Ilan Plain marks the western termination of the Okinawa trough that extends from southern Japan towards northern Taiwan. The extensional opening of the

Okinawa trough thus projects westward into Taiwan to form the Ilan Plain (Ho, 1982). Continuous subsidence due to crustal extension has resulted in recent alluvial deposits in the Ilan Plain.

Northeastern Taiwan is a tectonically complicated region. The Philippine Sea plate is moving northwest relative to the Eurasia plate, resulting in the Taiwan collision zone. The Philippine Sea plate subducts beneath the Eurasia plate along the Ryukyu arc. Most of the Ryukyu trench strikes northeast–southwest but turns to an east–west orientation for the segment west of 125° E. Morphology of the Ryukyu trench disappears to the west of 123° E, where it is intercepted by the Gagua ridge (Kao, 1998; Kao and Rau, 1999).

Selection of Earthquakes and Their Strong-Motion Data

Strong seismic ground-motion data were obtained by the TSMIP network operated by the Central Weather Bureau (CWB) of Taiwan. The TSMIP network has been designed to enhance the ability to monitor strong earthquakes and to collect high-quality instrumental recordings of free-field ground shaking (Liu *et al.*, 1999). Currently, the TSMIP accelerograph network consists of more than 700 free-field stations. It is one of the densest networks of digital strong-motion instruments in the world. For comparison, station spacing of the free-field accelerographs in the Ilan area of Taiwan is about 3–5 km, versus a 25-km uniform spacing of the K-NET in Japan (Bolt and Abrahamson, 2004; Liu and Tsai, 2005). Information about the 65 free-field TSMIP stations in Ilan area used in this study are given in Table 1, with their locations shown in Figure 2.

A total of 2852 digital accelerograms recorded from 92 shallow earthquakes, as given in Table 2, were selected for this study. The locations of these earthquakes are shown in Figure 1. Their M_w magnitudes range from 4.0 to 7.7. Some of the large earthquakes had caused serious damage in heavily populated areas. To address the site-based hazard representation, close moderate shallow earthquakes were also selected for this study. Specifically, the earthquakes and their recordings were selected according to the following criteria:

1. focal depths less than 35 km;
2. events recorded at more than 20 stations;
3. the recorded PGA greater than 8 cm/s² (i.e., CWB Intensity 3);
4. local magnitude, M_L , greater than 4.

In this study, the earthquake size is represented by the moment magnitude (M_w). In the CWB earthquake catalog, all events are given a local magnitude, which normally saturates at a value of about 6.5 (Heaton *et al.*, 1986; Reiter, 1991). Therefore, whenever available, we have adopted the moment magnitude from the Global Centroid Moment Tensor (CMT) Project database (Table 2). For earthquakes, mostly smaller than M_w 5.3, not reported by the Global CMT Project we

used the following empirical equation (Chen and Tsai, 2008) to convert M_L to M_w :

$$M_L = -0.24 + 1.07M_w, \quad (1)$$

where M_L is the local magnitude and M_w is the moment magnitude, respectively.

Table 2 also gives the rake angles for the earthquakes in the data set, using the convention of Aki and Richards (1980). The reverse-slip earthquakes have positive rake angles and the absolute value of the rake for left-lateral slip is less than 90°. We followed the definition by Boore *et al.* (1997) to classify a strike-slip earthquake as having a rake angle within 30° of the horizontal direction. The fault-type classification criteria for this study are given in Table 3. The number of earthquakes with available fault classifications of the reverse, strike-slip, and normal faulting types are 35, 23, and 29, respectively. The epicenters of earthquakes used in this study are shown in Figure 1 with the symbols representing different fault types. The open circle, triangle, and cross represent the style of faulting for reverse, strike-slip, and normal fault, respectively.

The distribution of data used to develop our model is shown in Figure 3a–d by magnitude and distance, respectively, for all faults and the three different fault types. The M_w magnitudes range from 4.0 to 7.7, and the distances range from 6.39 to 182.25 km. The numbers of records, available for all faults and the three fault types, are 2852, 1179, 831, and 725, respectively.

In summary, the shallow earthquakes that we selected for this study may be attributed to continental deformation, shallow collision, backarc opening, and uppermost plate interface, in the focal depth range of 2.0–31.3 km. Most earthquakes are shallower than 20 km.

Methodology

A strong-motion attenuation relationship expresses an earthquake ground-motion parameter as a function of simple parameters characterizing the earthquake source, the propagation path between the earthquake source and the site, and the geologic conditions beneath the site. Two models of equation forms used in this study are as follows (Boore *et al.*, 1993, 1997; Boore, 2005; Liu and Tsai, 2005; Douglas, 2011):

Model 1.

Phase 1: Includes only magnitude and distance terms

$$\ln(\text{PGA}, \text{PGV}) = c_1 + c_2(M_i - 6) + c_3(M_i - 6)^2 + c_4 \ln(X_{i,j} + h_1 \exp^{h_2 M_i}) + c_5 X_{i,j}. \quad (2)$$

Phase 2: Includes additional fault-type terms

$$\ln(\text{PGA}, \text{PGV}) = c_1 + c_2(M_i - 6) + c_3(M_i - 6)^2 + c_4 \ln(X_{i,j} + h_1 \exp^{h_2 M_i}) + c_5 X_{i,j} + (a_{SS}(M_i - 6) + b_{SS})\delta_{SS} + (a_{RV}(M_i - 6) + b_{RV})\delta_{RV} + (a_{NM}(M_i - 6) + b_{NM})\delta_{NM}. \quad (3)$$

Table 1
TSMIP Stations in Ilan Area Used in This Study

Number	Station Code	Latitude (° N)	Longitude (° E)	Elevation (m)	Site*	V_{530} (m/s)	Site [†]
1	ILA001	24.883	121.835	10	D	939.12	B
2	ILA002	24.845	121.796	10	D	220.68	D
3	ILA003	24.798	121.782	2	E	265.55	D
4	ILA004	24.745	121.782	2	E	121.45	E
5	ILA005	24.699	121.804	2	E	237.21	D
6	ILA006	24.641	121.824	8	E	276.37	D
7	ILA007	24.594	121.845	5	D		
8	ILA008	24.709	121.763	5	E	290.70	D
9	ILA010	24.619	121.781	45	D		
10	ILA011	24.831	121.740	250	B		
11	ILA012	24.781	121.734	12	D	255.48	D
12	ILA013	24.735	121.729	10	D	204.65	D
13	ILA014	24.695	121.719	20	D	322.17	D
14	ILA015	24.781	121.691	105	B	776.80	B
15	ILA016	24.750	121.683	35	D	269.71	D
16	ILA017	24.722	121.680	30	D	627.42	C
17	ILA018	24.682	121.680	50	D	497.47	C
18	ILA019	24.644	121.693	200	B		
19	ILA020	24.756	121.627	100	B	453.55	C
20	ILA021	24.713	121.645	80	D		
21	ILA022	24.669	121.643	90	D		
22	ILA023	24.684	121.599	165	D		
23	ILA024	24.662	121.611	300	B		
24	ILA025	24.638	121.563	279.9	B		
25	ILA026	24.675	121.765	3	D	237.50	D
26	ILA027	24.691	121.759	7	D	238.68	D
27	ILA028	24.756	121.747	5	D	218.38	D
28	ILA029	24.773	121.746	6	D	186.97	D
29	ILA030	24.728	121.756	4	E	198.51	D
30	ILA031	24.599	121.832	20	B	657.39	C
31	ILA032	24.623	121.828	5	D	296.52	D
32	ILA033	24.864	121.820	2	D	253.57	D
33	ILA034	24.804	121.806	3	E	217.67	D
34	ILA035	24.824	121.760	25	D	293.10	D
35	ILA036	24.789	121.752	4	D	179.02	E
36	ILA037	24.745	121.715	11	D	212.93	D
37	ILA038	24.721	121.735	9	D	243.85	D
38	ILA039	24.766	121.722	13	D	222.81	D
39	ILA040	24.774	121.791	2	E	188.35	D
40	ILA041	24.724	121.792	4	E	194.18	D
41	ILA042	24.689	121.790	4	E	213.18	D
42	ILA043	24.629	121.735	120	B		
43	ILA044	24.656	121.755	7	D	156.80	E
44	ILA046	24.667	121.734	60	D	393.83	C
45	ILA047	24.645	121.786	2	D		
46	ILA048	24.767	121.762	1	E	192.12	D
47	ILA049	24.766	121.748	7.2	D	202.32	D
48	ILA050	24.428	121.740	113	B	626.57	C
49	ILA051	24.720	121.675	20	B	535.24	C
50	ILA052	24.610	121.851	20	B		
51	ILA053	24.331	121.731	19	D	534.66	C
52	ILA054	24.972	121.918	53	B	771.41	B
53	ILA055	24.738	121.809	2	E	265.96	D
54	ILA056	24.761	121.808	2	E	221.29	D
55	ILA057	24.807	121.741	95	B		
56	ILA058	24.677	121.750	5	D		
57	ILA059	24.667	121.821	8	E	232.24	D
58	ILA060	24.578	121.836	4	D		
59	ILA061	24.523	121.825	15	D	502.05	C
60	ILA062	24.468	121.792	39	D		
61	ILA063	24.490	121.419	310	B	1002.6	B

(continued)

Table 1 (Continued)

Number	Station Code	Latitude (° N)	Longitude (° E)	Elevation (m)	Site*	V_{S30} (m/s)	Site†
62	ILA064	24.478	121.777	150	D		
63	ILA065	24.473	121.769	43	D		
64	ILA066	24.447	121.770	52	D	477.63	C
65	ILA067	24.439	121.373	1140			
66	ILA069	24.841	121.936	2.5			

*Determined by Lee *et al.* (2001) on the basis of surface geology and borehole data.

†According to UBC 1997.

Model 2.

Phase 1: Includes only magnitude and distance terms

$$\ln(\text{PGA, PGV}) = c_1 + c_2(M_i - 6) + c_3(M_i - 6)^2 + c_4 \ln(X_{i,j} + h_1 \exp^{h_2 M_i}) + c_5 X_{i,j}. \quad (4)$$

Phase 2: Includes an additional site term (V_{S30})

$$\ln(\text{PGA, PGV}) = c_1 + c_2(M_i - 6) + c_3(M_i - 6)^2 + c_4 \ln(X_{i,j} + h_1 \exp^{h_2 M_i}) + c_5 X_{i,j} + c_6 \ln(V_{S30}/760). \quad (5)$$

Phase 3: Includes additional site (V_{S30}) and fault-type terms

$$\begin{aligned} \ln(\text{PGA, PGV}) = & c_1 + c_2(M_i - 6) + c_3(M_i - 6)^2 + c_4 \ln(X_{i,j} \\ & + h_1 \exp^{h_2 M_i}) + c_5 X_{i,j} + c_6 \ln(V_{S30}/760) \\ & + (a_{SS}(M_i - 6) + b_{SS})\delta_{SS} + (a_{RV}(M_i - 6) \\ & + b_{RV})\delta_{RV} + (a_{NM}(M_i - 6) + b_{NM})\delta_{NM}. \end{aligned} \quad (6)$$

Subscript i is the i th earthquake, and subscript j is the j th record in the i th earthquake. In these equations, PGA and PGV are ground-motion parameters, and $X_{i,j}$ is the closest

distance to the rupture surface or hypocentral distance. We characterize the source-to-site distance in terms of the closest distance to the rupture surface, r_{rup} . If the rupture surface is not defined for an event, then the hypocentral distance is used as the source-to-site distance. M_i is moment magnitude (M_w), c_1 is a constant for all records, c_2 and c_3 are the magnitude scaling terms for all events, c_4 is the geometrical spreading coefficient, c_5 is the anelastic attenuation coefficient, h_1 and h_2 are close-in distance saturation coefficients. The $V_{\text{ref}} (= 760 \text{ m/s})$ is the specified reference velocity, corresponding to NEHRP B/C boundary site conditions. Subscript *SS* denotes strike-slip faulting, *RV* denotes reverse faulting, and *NM* denotes normal faulting. Dummy variables δ_{SS} , δ_{RV} , and δ_{NM} are for strike-slip, reverse, and normal-faulting events and take 0 or 1.

In this study, the maximum likelihood estimate and mixed-effects model are adopted in nonlinear regression for these equations. The processing was done using the nlme module in statistical software R (Pinheiro *et al.*, 2011). The initial coefficients in the equation for predicting ground motion were determined by using a two-stage regression procedure. A similar approach was used previously by Joyner and Boore (1993) and Liu and Tsai (2005).

We characterized the earthquake size by moment magnitude, M_w , as defined by Hanks and Kanamori (1979). We prefer M_w to surface-wave magnitude or local magnitude because M_w corresponds to well-defined physical properties of the source. Furthermore, the use of moment magnitude will avoid possible ‘‘saturation’’ of the more traditional band-limited magnitude measures for large earthquakes. Therefore, M_w is considered to be a better measure of the true size of an earthquake (Campbell, 1997).

We characterize the source-to-site distance in terms of the closest distance to the rupture surface, r_{rup} . If the rupture surface was not defined for an event, then hypocentral distance was used as the source-to-site distance. This was particularly true for many of the smaller magnitude events. Because the dimensions of the rupture surface for small events are usually much smaller than the distances to the recording stations, we believe that the use of hypocentral distance will not introduce significant bias into the attenuation relationships (Sadigh *et al.*, 1997; Youngs *et al.*, 1997).

The two models are adopted to account for different situations. Model 1, using recordings from all 65 strong-motion sites, is especially useful for early warning systems to make

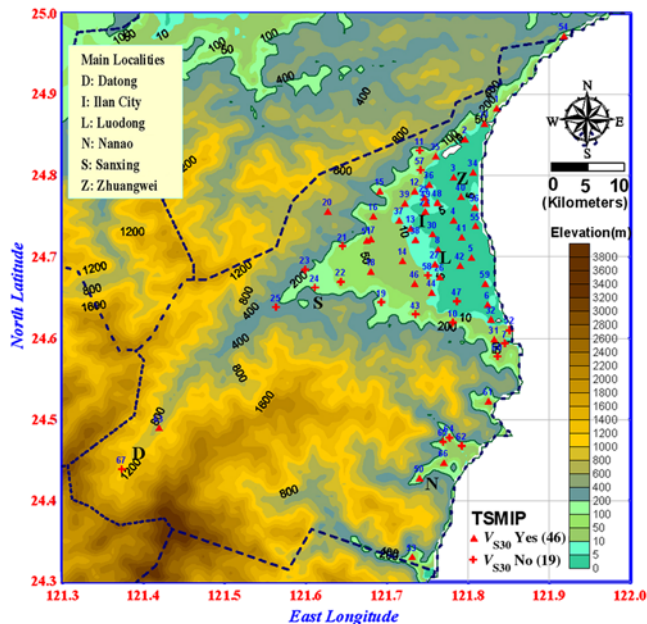


Figure 2. Distribution of the TSMIP free-field stations in the Ilan area used in this study. The dashed lines in the map mark the boundaries of counties. Main localities are also indicated by bold letters. The color version of this figure is available only in the electronic edition.

Table 2
Earthquakes Used in This Study

Number	Date (yyyy/mm/dd)	Time (hh/mm/ss.ss)	Latitude (° N)	Longitude (° E)	Depth (km)	M_L	M_w	Rake	Fault Type [†]	Record Number
1	1994/04/30	9:14:17.12	24.354	122.074	3.9	5.04	4.93	—		25
2	1994/05/23	15:16:58.75	23.863	122.636	5.54	6	5.9*	79	RC	23
3	1994/05/24	4:00:40.49	23.827	122.603	4.45	6.6	6.5*	-66	N	29
4	1994/06/05	1:09:30.09	24.462	121.838	5.3	6.5	6.4*	-6	N	37
5	1994/06/06	8:57:24.49	24.431	121.949	3.45	5.06	4.95	—		25
6	1994/10/28	23:51:10.48	24.636	122.270	2	5.66	5.6*	-63	N	28
7	1994/11/26	11:17:35.62	24.637	122.225	3.77	5.54	5.40	-59	N	29
8	1995/02/23	5:19:02.78	24.204	121.687	21.69	5.77	6.2*	75	RB	37
9	1995/04/03	11:54:40.08	23.936	122.432	14.55	5.88	5.7*	76	RC	23
10	1995/07/14	16:52:46.48	24.320	121.851	8.79	5.8	5.64	0	S	33
11	1995/12/18	16:17:54.53	24.018	121.692	22.06	5.8	5.3*	72	RB	27
12	1996/03/05	14:52:27.13	23.930	122.362	6	6.4	6.3*	75	RC	47
13	1996/08/10	6:23:05.69	23.885	122.650	5.65	5.76	5.7*	64	RC	27
14	1996/11/26	8:22:23.71	24.164	121.695	26.18	5.35	5.2*	20	S	37
15	1997/01/05	10:34:16.85	24.623	122.530	1.13	5.78	5.2*	-85	N	34
16	1997/04/02	22:36:41.85	24.688	121.745	11.95	4.33	4.27	-70	N	39
17	1998/11/24	5:33:56.41	24.586	121.734	7.19	4.01	3.97	-56	N	24
18	1999/02/22	13:48:58.05	23.975	122.655	4.21	5.9	5.9*	72	RC	27
19	1999/05/07	1:03:24.41	24.739	121.892	4.17	5.44	5.31	-52	N	45
20	1999/05/07	12:24:41.87	24.749	121.857	10.08	4.13	4.08	-82	N	29
21	1999/05/08	7:52:48.02	24.776	121.878	9.76	4.27	4.21	—		27
22	1999/05/08	7:54:35.90	24.778	121.872	11.32	4.23	4.18	-74	N	22
23	1999/05/08	23:33:28.67	24.760	121.854	4.42	4.42	4.36	-85	N	37
24	1999/09/20	17:47:15.85	23.853	120.816	8	7.3	7.7*	87	RA	44
25	1999/09/20	17:57:15.58	23.912	121.044	7.68	6.44	6.24	78	RA	43
26	1999/09/20	18:02:19.81	24.234	121.133	7.1	5.41	5.28	—		20
27	1999/09/20	18:11:54.21	23.865	121.067	12.49	6.7	6.49	7	S	43
28	1999/09/20	18:16:17.95	23.862	121.041	12.53	6.66	6.9*	65	RA	38
29	1999/09/20	21:46:38.11	23.585	120.857	8.57	6.59	6.4*	1	S	26
30	1999/09/22	0:14:40.77	23.826	121.047	15.59	6.8	6.3*	55	RA	36
31	1999/09/22	0:49:43.45	23.765	121.031	17.38	6.2	5.8*	87	RA	32
32	1999/09/25	23:52:49.63	23.854	121.002	12.06	6.8	6.5*	88	RA	39
33	1999/11/01	17:53:02.25	23.362	121.726	31.33	6.9	6.3*	76	RB	41
34	2000/06/06	1:49:39.03	24.487	121.864	21.55	4.79	4.70	-20	S	22
35	2000/06/10	18:23:29.45	23.901	121.109	16.21	6.7	6.4*	51	RA	40
36	2000/06/19	21:56:24.76	23.920	121.092	27.02	5.18	5.3*	65	RA	21
37	2000/07/10	6:23:13.17	24.468	121.855	19.32	4.68	4.60	-30	N	20
38	2000/09/10	8:54:46.53	24.085	121.584	17.74	6.2	5.8*	63	RB	45
39	2000/11/20	0:07:09.37	24.794	121.910	8.58	4.81	4.72	-75	N	47
40	2000/12/29	18:03:28.59	24.361	121.884	6.96	5.26	5.14	-10	S	41
41	2001/01/22	23:27:18.27	24.319	122.134	13.1	5.16	5.05	29	S	30
42	2001/06/14	2:35:25.78	24.419	121.928	17.29	6.3	5.9*	-5	S	46
43	2001/06/30	4:07:37.73	24.055	121.543	23.37	4.96	4.86	-70	N	20
44	2001/12/18	4:03:00.75	23.867	122.652	12	6.7	6.8*	-53	N	49
45	2002/02/12	3:27:25.00	23.741	121.723	29.98	6.2	5.7*	65	RB	27
46	2002/03/31	6:52:49.95	24.140	122.192	13.81	6.8	7.1*	72	RC	43
47	2002/03/31	11:50:08.81	24.709	121.814	8.39	4.13	4.08	-80	N	30
48	2002/04/04	13:04:49.58	24.315	121.786	9.88	4.55	4.48	85	RB	20
49	2002/05/15	3:46:05.91	24.651	121.872	8.52	6.2	6.2*	-18	S	28
50	2002/05/15	4:42:41.26	24.657	121.844	10.05	4.62	4.4*	-30	N	20
51	2002/05/28	16:45:14.97	23.913	122.397	15.23	6.2	6.1*	79	RC	24
52	2002/06/13	20:40:27.83	24.775	122.133	8.14	5.03	5.2*	-73	N	23
53	2002/08/14	23:28:56.77	24.425	121.946	22.06	4.61	4.53	46	RC	26
54	2002/08/28	20:01:56.24	24.429	121.890	19.03	4.2	4.15	-8	S	25
55	2003/06/09	1:52:50.57	24.370	122.023	23.22	5.72	5.8*	82	RC	46
56	2003/06/09	5:08:04.68	24.380	121.851	2.36	5.03	4.93	23	S	36
57	2003/07/13	15:06:30.08	24.461	121.897	18.84	4.7	4.62	22	S	24
58	2003/11/12	0:02:35.91	24.453	121.953	21.29	5.39	5.26	55	RC	39
59	2004/07/06	7:32:02.77	24.897	122.266	5.96	5.22	5.2*	-84	N	25

(continued)

Table 2 (Continued)

Number	Date (yyyy/mm/dd)	Time (hh/mm/ss.ss)	Latitude (° N)	Longitude (° E)	Depth (km)	M_L	M_w	Rake	Fault Type [†]	Record Number
60	2004/09/07	11:45:55.18	24.653	121.852	12.77	4.05	4.01	-70	N	22
61	2004/11/08	15:54:55.86	23.795	122.760	10	6.58	6.3*	75	RC	41
62	2004/11/11	2:16:44.50	24.312	122.158	27.26	6.09	5.7*	64	RC	30
63	2005/02/01	1:59:47.77	24.256	121.780	5.74	5.14	5*	86	RB	32
64	2005/02/05	11:00:52.86	24.249	121.752	4.9	4.99	4.89	71	RB	39
65	2005/02/28	2:01:08.53	24.772	122.045	7.45	4.37	4.31	62	R	24
66	2005/03/05	18:59:17.40	24.646	121.828	9.95	4.01	3.97	-87	N	22
67	2005/03/05	19:06:51.73	24.655	121.841	6.39	5.9	5.8*	-26	S	45
68	2005/03/05	19:08:00.09	24.653	121.798	6.95	5.96	5.8*	-29	S	45
69	2005/03/05	19:12:23.22	24.665	121.825	9.68	4.14	4.09	—		23
70	2005/03/05	19:16:25.97	24.645	121.759	8.35	4.83	4.74	-21	S	41
71	2005/03/05	19:27:54.36	24.660	121.801	10.71	4.75	4.66	-20	S	36
72	2005/03/05	19:55:01.24	24.670	121.822	12.69	4	3.96	-44	N	21
73	2005/03/05	21:06:12.86	24.663	121.871	5.04	4.14	4.09	-60	N	28
74	2005/03/05	23:19:36.86	24.657	121.884	4.35	4.3	4.1*	-10	S	26
75	2005/03/07	19:26:25.52	24.647	121.820	8.22	4.31	4.25	-16	S	25
76	2005/07/20	13:06:03.54	24.751	122.255	7.6	5.22	5.3*	2	S	27
77	2005/09/03	12:52:15.20	24.813	121.889	8.75	4.31	4.25	-68	N	28
78	2006/02/24	1:55:50.23	24.778	122.228	12.56	5.17	4.8*	-82	N	21
79	2006/04/02	13:41:21.24	24.472	121.864	20.52	4.42	4.36	-9	S	28
80	2006/04/22	5:12:14.19	24.472	121.867	21.17	4.08	4.04	-51	N	20
81	2006/07/28	7:40:10.43	23.966	122.658	27.97	6.02	5.9*	64	RC	36
82	2006/10/12	14:46:29.29	23.964	122.645	25.26	5.8	5.8*	62	RC	24
83	2006/12/23	17:28:27.19	24.807	122.319	9.77	5.37	5.1*	-77	N	30
84	2007/06/20	14:21:45.09	24.397	121.830	12.34	4.05	4.01	10	S	20
85	2007/07/12	20:54:12.33	24.790	121.819	10.39	4.44	4.37	-37	N	41
86	2007/09/22	6:27:04.51	24.464	121.867	22.47	4.77	4.68	20	S	39
87	2008/05/03	13:17:08.61	24.443	121.888	20.51	4.50	4.43	-7	S	27
88	2009/06/28	9:34:56.19	24.182	121.753	12.88	5.26	5.1*	69	RB	32
89	2009/07/13	18:05:02.59	24.023	122.219	18.08	6.00	6.3*	73	RC	51
90	2009/10/03	17:36:06.28	23.648	121.579	29.15	6.09	5.9*	63	RB	34
91	2009/10/22	20:46:24.33	24.278	121.778	20.19	4.90	4.80	-72	N	39
92	2009/11/05	9:32:57.66	23.789	120.719	24.08	6.15	5.6*	39	RA	40

*The moment magnitude (M_w) adopted from the Global CMT Project.

†The letters R, S, and N stand for the reverse, strike-slip, and normal fault types, respectively. The letters RA, RB, and RC stand for the three source areas A, B, and C of reverse earthquakes, respectively.

quick assessment and timely reporting of the PGA and PGV maps. Their results will be critical for effective emergency-response operations. On the other hand, Model 2, using 46 strong-motion sites to incorporate a site-effect term with available V_{S30} , is aimed to reduce the standard deviation of the predicted ground motion. This approach emphasizes direct use of the recordings of strong ground motion for estimation of seismic ground shaking for engineering applications.

In addition, the residual value (i.e., site-response factor), is defined as the difference between logarithms of the

observed and the predicted ground motion, and is expressed by the following equation

$$r = \ln Y_S - \ln Y_r = \eta + \varepsilon, \tag{7}$$

where Y_S is the observed value, Y_r is the predicted value from equation (2), η is the earthquake interevent errors with standard deviation equal to τ , and ε is intraevent errors with standard deviation equal to σ . The η and ε are assumed to be independent normally distributed variants with variances τ^2 and σ^2 . The amplification factors of site effect can be calculated from $\exp(r)$. The standard deviation of total residual $\sigma_{T(T=1 \text{ or } 2)}$ is given by the equation

$$\sigma_T = \sqrt{\sigma^2 + \tau^2}. \tag{8}$$

The residuals due to regression were decomposed into interevent (earthquake-to-earthquake) and intraevent residuals. The interevent and intraevent residuals are calculated by equations (3.15) and (3.16) in Campbell and Bozorgnia (2007).

Table 3

Fault Type Classification Criteria for This Study (Aki and Richards, 1980)

Fault Type Class	Rake
Normal	-90 < rake < -30
Strike-slip	-30 < rake < 30
Reverse	30 < rake < 90

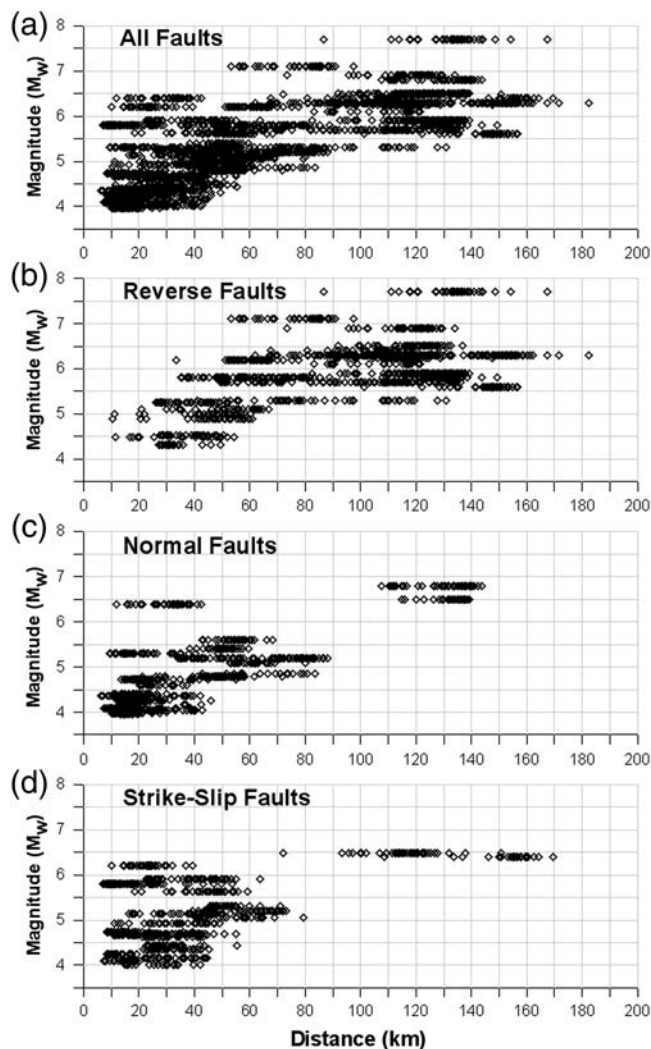


Figure 3. The distribution of data used to develop the attenuation relationships by magnitude and distance, according to different fault types.

Attenuation Relationships for Vertical and Horizontal PGA and PGV

Regressions on the data set of Model 1 without differentiating site conditions and Model 2 with site conditions have resulted in the coefficients of the attenuation relationships, as given in Tables 4–5 and 6–8, respectively, for the vertical and horizontal components of PGA and PGV in the Ilan area. In Tables 4–8, σ_1 and σ_2 are standard deviations on $\ln(\text{PGA}, \text{PGV})$. From these coefficients, we can find faster attenuation in the vertical component than the horizontal component of PGA. Moreover, PGA has faster attenuation than PGV for both the vertical and horizontal components.

Fault-Type Effect

To illustrate the style-of-faulting difference of ground-motion characteristics, Figures 4 and 5 show the mean

attenuation relationships of the horizontal PGA and PGV, respectively, as a function of distance for $M_w 7$ for all faults and the three fault types in the Ilan area. Apparently, the ground motions systematically differ when generated by strike-slip, reverse, or normal fault mechanisms. Given the same earthquake magnitude, distance, and site condition, the horizontal PGA (PGA_h) from reverse earthquakes tends to be larger than the PGA_h from normal-faulting earthquakes by about 33%. The PGA_h from strike-slip earthquakes tends to be smaller than the PGA_h from normal-faulting earthquakes by about 37%. In contrast, the lower frequency horizontal PGV (PGV_h) from reverse earthquakes tends to be larger than PGV_h from normal-faulting earthquakes by about 72%. The PGV_h from strike-slip earthquakes tends to be greater than the PGV_h from normal-faulting earthquakes by only about 2%.

V_{S30} Effect

Previously, most attenuation relationships used broad site categories, such as rock, stiff soil, and soft soil. Recently, there has been a move toward using more quantitative site classifications based on the shear-wave velocity measured at the strong-motion site. The most commonly used parameter is the average shear-wave velocity over the top 30 m (V_{S30} ; Boore *et al.*, 1997; Bolt and Abrahamson, 2004). In developing ground-motion models, developers systematically evaluated a list of predictor parameters to be included for predicting earthquake effects. One of the most significant consensus reached by all developers was to use the average shear-wave velocity in the upper 30 m of sediments (V_{S30}) as the parameter for characterizing soil-stiffness effects on ground motions (Power *et al.*, 2008).

The difficulty in using quantitative site descriptions is that the information is not always available for the majority of strong-motion sites that have recorded strong motions. This situation has been greatly improved for our study because shear-wave velocities were measured at 46 of the 65 strong-motion sites in Ilan area, as given in Table 1. Incorporating the average shear-wave velocity over the top 30 m (V_{S30}) into the attenuation relationship with a site-effect term, the typical forms we used in this study are given in equations (2), (4), and (5).

Figure 6 shows the mean attenuation relationships of the vertical and horizontal PGA and PGV as a function of distance for $M_w 7$ from Model 1 (equation 2) and Model 2 (equation 4). The figure shows that the curves of horizontal PGA and vertical PGV in Model 1 lie close to those of Model 2. On the other hand, we can see that the horizontal PGV of Model 2 has higher values than that of Model 1. This is because the percentage of station records from soil sites (D and E) used to derive attenuation relationships 69.6% (32/46) in Model 2 is higher than 58.5% (38/65) in Model 1. In contrast, the vertical PGA of Model 1 has higher values than that of Model 2. This is because the percentage of station records from rock site

Table 4
Coefficients for the Vertical and Horizontal Components of PGA and PGV in Equation (2) from Model 1, Phase 1

		c_1	c_2	c_3	c_4	h_1	h_2	c_5	a_{SS}	b_{SS}	a_{RV}	b_{RV}	a_{NM}	b_{NM}	σ_1	
PGA	V-Comp.	10.225	1.217	-0.095	-1.707	1.943	0.169	-0.0036								0.612
	H-Comp.	9.383	1.177	-0.070	-1.258	2.446	0.187	-0.0071								0.609
PGV	V-Comp.	5.039	1.646	-0.032	-1.146	0.764	0.284	-0.0012								0.592
	H-Comp.	6.096	1.637	-0.079	-1.145	0.359	0.534	-0.0024								0.668

Model 1, Phase 1 (includes only magnitude and distance terms).

Table 5
Coefficients for the Vertical and Horizontal Components of PGA and PGV in Equation (3) from Model 1, Phase 2

		c_1	c_2	c_3	c_4	h_1	h_2	c_5	a_{SS}	b_{SS}	a_{RV}	b_{RV}	a_{NM}	b_{NM}	σ_1
PGA	V-Comp.	10.740	1.712	-0.092	-1.718	1.943	0.169	-0.0036	-0.769	-0.790	-0.509	-0.358	-0.504	-0.550	0.596
	H-Comp.	9.820	1.631	-0.063	-1.272	2.446	0.187	-0.0071	-0.685	-0.658	-0.479	-0.259	-0.496	-0.531	0.593
PGV	V-Comp.	5.131	1.807	-0.040	-1.161	0.764	0.284	-0.0012	-0.387	-0.326	-0.192	0.128	-0.269	-0.231	0.573
	H-Comp.	6.046	1.721	-0.077	-1.163	0.359	0.534	-0.0024	-0.267	-0.092	-0.125	0.284	-0.211	-0.175	0.649

Model 1, Phase 2 (adds fault-type term).

Table 6
Coefficients for the Vertical and Horizontal Components of PGA and PGV in Equation (4) from Model 2, Phase 1

		c_1	c_2	c_3	c_4	h_1	h_2	c_5	c_6	a_{SS}	b_{SS}	a_{RV}	b_{RV}	a_{NM}	b_{NM}	σ_2
PGA	V-Comp.	9.773	1.201	-0.073	-1.612	1.943	0.169	-0.0036								0.572
	H-Comp.	9.343	1.216	-0.056	-1.243	2.446	0.187	-0.0071								0.599
PGV	V-Comp.	4.960	1.679	-0.020	-1.122	0.764	0.284	-0.0012								0.582
	H-Comp.	6.465	1.715	-0.076	-1.205	0.359	0.534	-0.0024								0.655

Model 2, Phase 1 (includes only magnitude and distance terms).

Table 7
Coefficients for the Vertical and Horizontal Components of PGA and PGV in Equation (5) from Model 2, Phase 2

		c_1	c_2	c_3	c_4	h_1	h_2	c_5	c_6	a_{SS}	b_{SS}	a_{RV}	b_{RV}	a_{NM}	b_{NM}	σ_2
PGA	V-Comp.	9.782	1.199	-0.072	-1.608	1.943	0.169	-0.0036	0.027							0.571
	H-Comp.	9.333	1.222	-0.059	-1.256	2.446	0.187	-0.0071	-0.073							0.601
PGV	V-Comp.	4.885	1.698	-0.028	-1.157	0.764	0.284	-0.0012	-0.245							0.575
	H-Comp.	6.393	1.767	-0.094	-1.301	0.359	0.534	-0.0024	-0.536							0.613

Model 2, Phase 2 (adds site term V_{S30}).

Table 8
Coefficients for the Vertical and Horizontal Components of PGA and PGV in Equation (6) from Model 2, Phase 3

		c_1	c_2	c_3	c_4	h_1	h_2	c_5	c_6	a_{SS}	b_{SS}	a_{RV}	b_{RV}	a_{NM}	b_{NM}	σ_2
PGA	V-Comp.	10.341	1.717	-0.071	-1.625	1.943	0.169	-0.0036	0.027	-0.749	-0.750	-0.522	-0.391	-0.537	-0.573	0.559
	H-Comp.	9.877	1.727	-0.050	-1.279	2.446	0.187	-0.0071	-0.073	-0.708	-0.719	-0.531	-0.327	-0.550	-0.608	0.586
PGV	V-Comp.	4.910	1.819	-0.036	-1.178	0.764	0.284	-0.0012	-0.246	-0.324	-0.220	-0.158	0.223	-0.245	-0.165	0.555
	H-Comp.	6.305	1.869	-0.084	-1.319	0.359	0.534	-0.0024	-0.536	-0.278	-0.073	-0.166	0.335	-0.228	-0.158	0.587

Model 2, Phase 3 (adds site term V_{S30} and fault-type term).

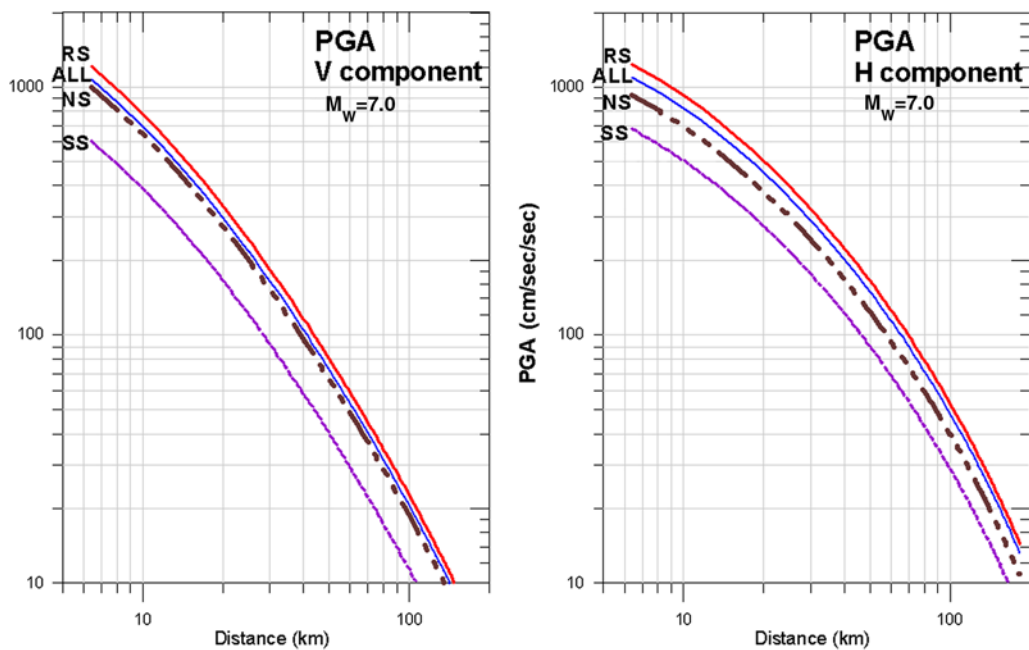


Figure 4. The mean attenuation relationships of the vertical and horizontal PGA as a function of distance for M_w 7 for all faults and the three fault types in the Ilan area. The color version of this figure is available only in the electronic edition.

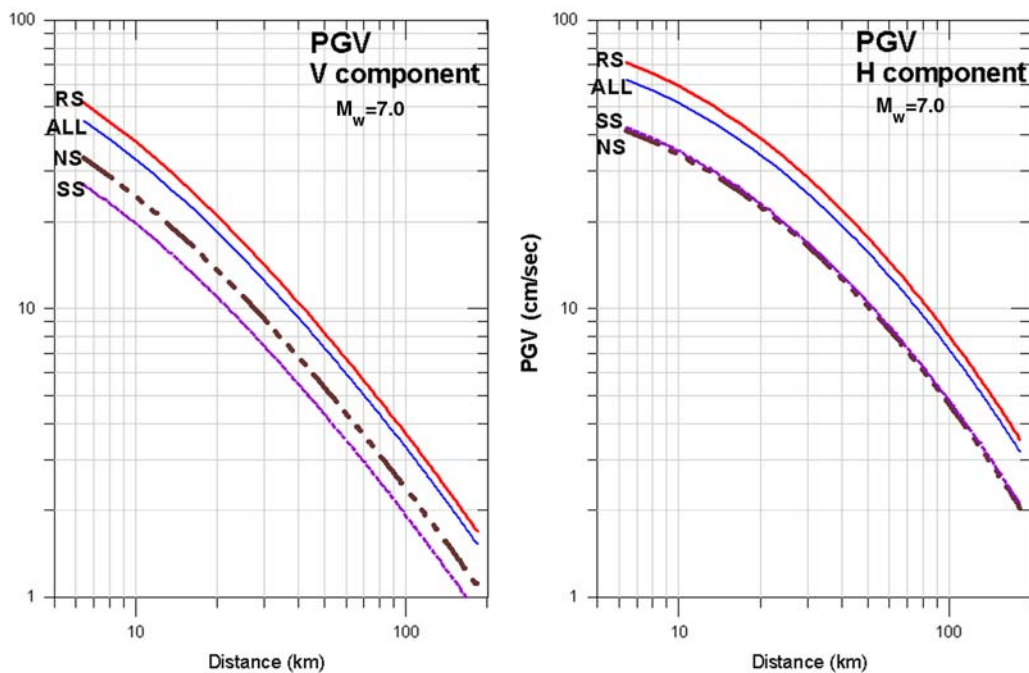


Figure 5. The mean attenuation relationships of the vertical and horizontal PGV as a function of distance for M_w 7 for all faults and the three fault types in the Ilan area. The color version of this figure is available only in the electronic edition.

(B and C) used to derive attenuation relations 41.5% (27/65) in Model 1 is higher than 30.4% (14/46) in Model 2.

Furthermore, we analyze the correlation between the intraevent residual of attenuation relationship and V_{S30} before and after incorporating the site-effect term, V_{S30} in Model 2 (equations 4 and 5). The intraevent residuals as a function of V_{S30} before incorporating the site-effect term for the hori-

zontal PGA and PGV, respectively, are plotted in Figure 7a,b. The solid lines represent the linear regression function. The coefficient of determination R^2 , slope of the trend line, median value, and the associated standard deviation are also shown in the figure. R is the correlation coefficient used to measure how much linear relationship exists between the values for the two variables. R can range between +1

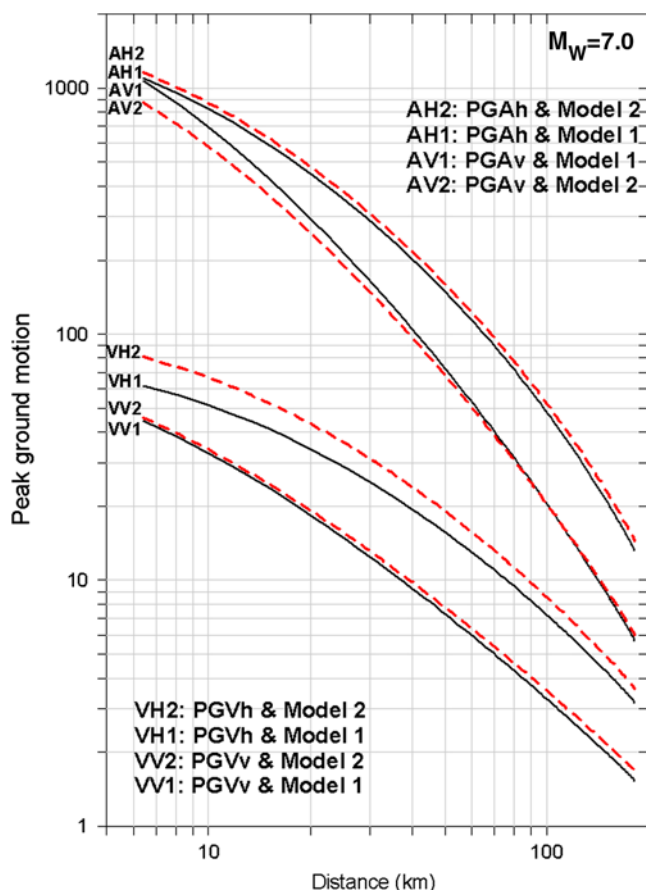


Figure 6. The mean attenuation relationships of the vertical and horizontal PGA and PGV as a function of distance for M_w 7 from Model 1 (equation 2) and Model 2 (equation 4). The color version of this figure is available only in the electronic edition.

and -1 . A value near zero means that there is a random, non-linear relationship between the two variables. It is clear from Figure 7a,b that the PGV residual is much more sensitively related to the V_{S30} than the PGA residual.

On the other hand, Figure 7c,d shows the residuals as a function of V_{S30} after incorporating the site-effect term for the horizontal PGA and PGV, respectively. Reading from Figure 7b,d the original values of R and the slope were 0.497 ($R^2 = 0.2472$) and -0.515 , respectively, indicating that the PGV residual has a high contribution from the V_{S30} term before incorporating the site-effect term into the attenuation relationship. However, the R and slope value were reduced to 0.000 ($R^2 = 0.0000$) and 0.000 , respectively, after incorporating the site-effect term into the attenuation relationship. Obviously, the attenuation relationship was improved by including the site-effect term.

Comparisons of Model Predictions by Sigma and Akaike Information Criterion

As our understanding and modeling of attenuation relationships improve, there will be a trend toward reducing the modeling variability. In empirical attenuation models, the mod-

eling variability given is the standard deviation (Bolt and Abrahamson, 2004). In addition to the median ground motion, the standard deviation (σ) of ground motion is also important for seismic-hazard analyses. In addition, we also use Akaike Information Criterion (AIC) to confirm their statistical significance. AIC stands for an information theoretic criterion and is a measure of the best models under the minimum amount of controlling parameters (Akaike, 1974).

The standard deviations (σ) and AIC for different phases in Models 1 and 2 are given in Table 9 and plotted in Figures 8 and 9, respectively. From Figure 8 (Model 1), we can find all σ values decrease by $1.7\% \sim 3.3\%$ from Phase 1 to Phase 2 after adding the fault-type term in vertical and horizontal PGA and PGV. Likewise, from Figure 9 (Model 2), all σ values also decrease by $2.1\% \sim 4.4\%$ from Phase 2 to Phase 3 after adding the fault-type term in vertical and horizontal PGA and PGV. However, from Phase 1 to Phase 2 after adding the site term (V_{S30}) in Model 2, the σ values changed by a percentage value of $-0.2\% \sim 6.9\%$ in vertical and horizontal PGA and PGV.

After incorporating the site-effect term, V_{S30} , in the attenuation relationships, the standard deviations of the residuals between the observed and predicted values changed from 0.599 to 0.600 for horizontal PGA and from 0.655 to 0.613 for horizontal PGV, respectively. We found the change of standard deviation for PGA is not obvious. In contrast, the PGV standard deviation is significantly reduced by 6.9% . In summary, all σ values decrease by $2.2\% \sim 11.6\%$ from Phase 1 to Phase 3 in Model 2 after adding the site term (V_{S30}) and fault-type term in vertical and horizontal PGA and PGV. Obviously, the attenuation relationships were improved by including the site-effect and fault-type terms. Phase 3 (equation 6) has reduced the modeling variability (standard deviation) and is considered to be more appropriate for engineering purposes.

Furthermore, we also use AIC to confirm their statistical significance. During the first step of development in Model 1, only the magnitude and distance terms are included in the model. The results show that the AIC equals 4017.50 and 4635.06 , respectively, for horizontal PGA and PGV. Next, three fault-type terms are added individually to the model. The results show only slight improvement: the AIC decreases to 4016.35 and 4632.31 , respectively. The detailed results for all vertical and horizontal PGA and PGV are given in Table 9. Clearly, inclusion of the fault type in the attenuation model has slight statistical significance and does reduce the regression error, thus resulting in a smaller AIC.

Similarly, during the first step of development in Model 2, only the magnitude and distance terms are included in the model. The results show that the AIC equals 2953.20 and 3303.27 , respectively, for horizontal PGA and PGV. The detailed results for both vertical and horizontal PGA and PGV are given in Table 9. Next, the site term was added to the model using the V_{S30} . The results again show great improvement: the AIC equals 2700.76 in horizontal PGV. However, the inclusion of V_{S30} in the attenuation model is not

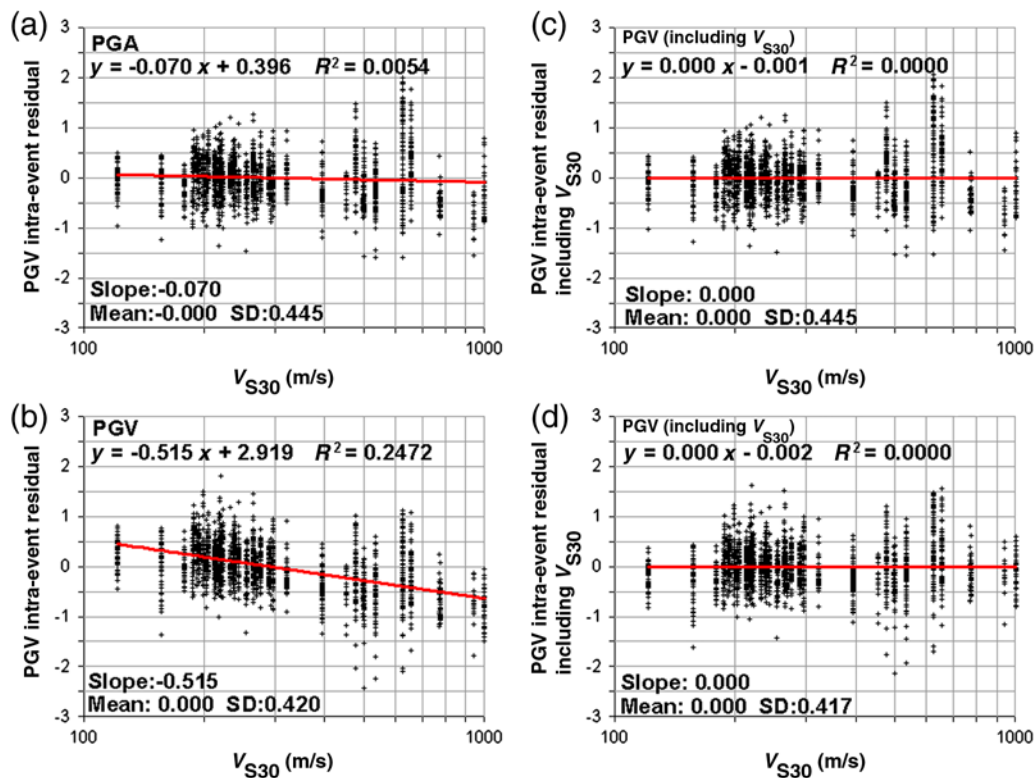


Figure 7. (a) and (b) The intraevent residual as a function of V_{S30} before incorporating the site-effect term for the horizontal PGA and PGV, respectively. The solid lines represent the linear regression function. (c) and (d) The intraevent residual as a function of V_{S30} after incorporating the site-effect term for the horizontal PGA and PGV, respectively. The coefficient of determination R^2 , slope of the trend line, median value, and the associated standard deviation are also shown in the figures. The color version of this figure is available only in the electronic edition.

statistically significant in vertical and horizontal PGA. Clearly, inclusion of V_{S30} in the PGV attenuation model is statistically significant and does reduce the regression error, thus resulting in a smaller AIC. In contrast, inclusion of the V_{S30} term in the PGA attenuation model is not statistically significant. Last, three fault-type terms are added individually to the model. The results show slight improvement as the AIC decreases to 2695.83 in horizontal PGV. Accordingly, inclusion of the fault type in the attenuation model has slight statistical significance.

Comparisons of Attenuation Models between This Study and NGA

The attenuation relationships of horizontal PGA as a function of distance for M_w 6 and $V_{S30} = 760$ m/s for the Ilan area in northeastern Taiwan are compared with the NGA models as shown in Figure 10 (Abrahamson and Silva, 2008; Boore and Atkinson, 2008; Campbell and Bozorgnia, 2008; Chiou and Youngs, 2008). Figure 10a–c shows the strike-slip, normal, and reverse fault, respectively. The figure shows the pattern of Ilan curves is similar to CY08. Moreover, the Ilan curves have higher values than the NGA models in closer distances (within 45 ~ 75 km), especially for the

normal fault. In our study, the PGA values produced for the normal faults are higher than those for strike-slip faults. This result is further supported later in this paper by the analysis of fault-type residual.

In addition, Figure 11 shows the mean attenuation relationships of the horizontal PGA as a function of distance for M_w 6 of the strike-slip faults for the Ilan area and the four NGA models. Figure 11a–c shows the cases with $V_{S30} = 360$ m/s, 760 m/s, and 1100 m/s, respectively. The figure also shows that the pattern of Ilan curves is similar to CY08. Additionally, it is noted that horizontal PGA at near-source distances (within 25 ~ 56 km) has higher values for the Ilan area than those for the four NGA models.

Analysis of Residuals

A more precise way of looking for systematic errors between predictions and observations is to plot the residuals, defined as the difference between logarithms of the observed and predicted ground motion by equation (7). We analyzed the residuals to investigate variations of PGA and PGV with respect to fault type and site effect (V_{S30}) in the following section.

Table 9
Standard Deviations and AIC Values from Different Phases of Models 1 and 2

		Variables Description	Component		Interevent Sigma (τ)	Intraevent Sigma (ϵ)	Total Sigma (σ)	AIC*
Model 1	Phase 1	Only magnitude and distance terms	PGA	V	0.412	0.452	0.612	3877.30
				H	0.394	0.464	0.609	4017.50
			PGV	V	0.382	0.451	0.592	3853.64
	Phase 2	Add fault-type term	PGA	V	0.422	0.518	0.668	4635.06
				H	0.388	0.452	0.596	3877.29
			PGV	V	0.369	0.464	0.593	4016.36
Model 2	Phase 1	Only magnitude and distance terms	PGA	V	0.353	0.451	0.573	3849.82
				H	0.391	0.518	0.649	4632.31
			PGV	V	0.377	0.430	0.572	2715.95
	Phase 2	Add site term (V_{S30})	PGA	H	0.389	0.456	0.599	2953.20
				V	0.378	0.442	0.582	2826.12
			PGV	H	0.429	0.494	0.655	3303.27
	Phase 3	Add site term (V_{S30}) and fault-type term	PGA	V	0.376	0.430	0.571	2716.16
				H	0.393	0.454	0.600	2934.82
			PGV	V	0.385	0.427	0.575	2685.94
			PGA	H	0.441	0.426	0.613	2700.76
				V	0.357	0.430	0.559	2717.06
			PGV	H	0.371	0.454	0.586	2934.27
			PGV	V	0.355	0.426	0.555	2681.75
				H	0.404	0.426	0.587	2695.83

*Akaike information criterion (Akaike, 1974).

Fault-Type Residuals

The fault-type parameter is used to distinguish the effects of different source types. Figure 12a–d shows the interevent residuals as a function of magnitude in different fault types for the horizontal components of PGA in the Ilan area. The dashed lines represent baseline for residual equal to zero, while the solid lines represent the linear regression functions. From these figures, interevent residual decreases

with increasing magnitude faster in the strike-slip fault type than the reverse and normal fault types.

Similarly, we also plot interevent residuals as a function of magnitude in different fault types for the vertical and horizontal components of PGA and PGV in the Ilan area. The total regression functions are shown in Figure 13a–d, and the corresponding regression coefficients are given in Table 10. In Table 10, Residuals are represented as R_{SS} , R_{RS} , R_{NS} , and R_{ALL} for strike-slip, reverse-slip, and normal-slip

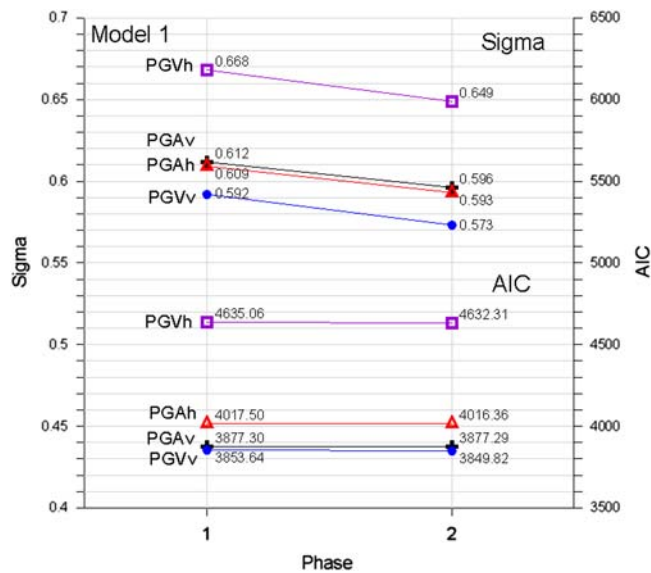


Figure 8. The standard deviations (sigma) and AIC values from different phases of Models 1. The color version of this figure is available only in the electronic edition.

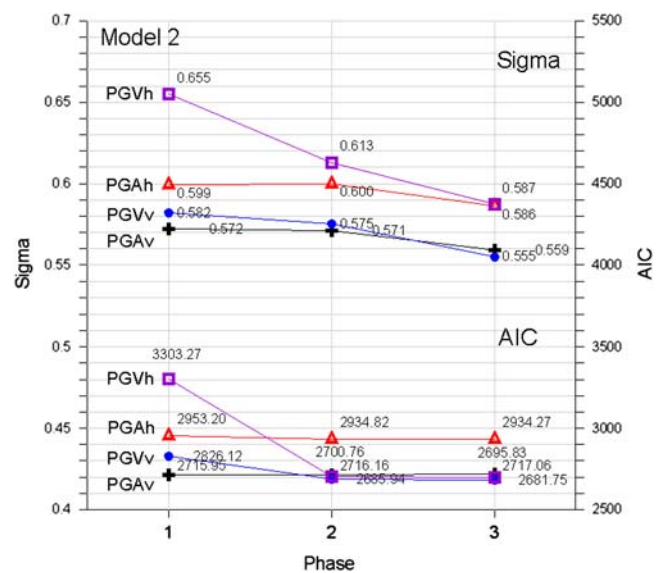


Figure 9. The standard deviations (sigma) and AIC values from different phases of Models 2. The color version of this figure is available only in the electronic edition.

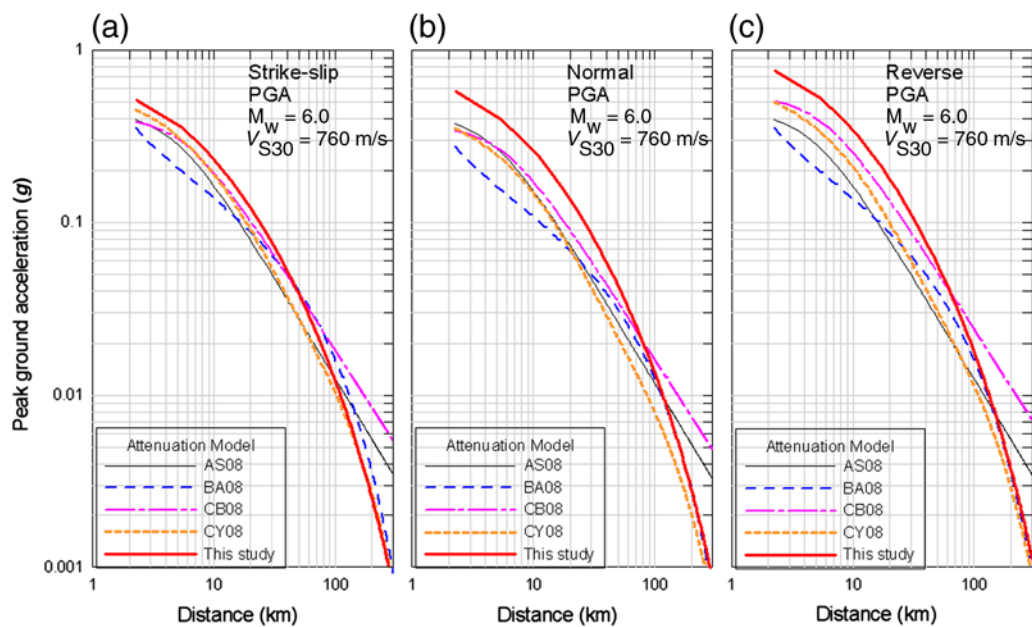


Figure 10. Plots of the mean attenuation relationships of horizontal PGA as a function of distance for M_w 6 and $V_{S30} = 760$ m/s for the Ilan area in northeastern Taiwan, as compared with the NGA models. (a–c) The strike-slip, normal, and reverse fault, respectively. The color version of this figure is available only in the electronic edition.

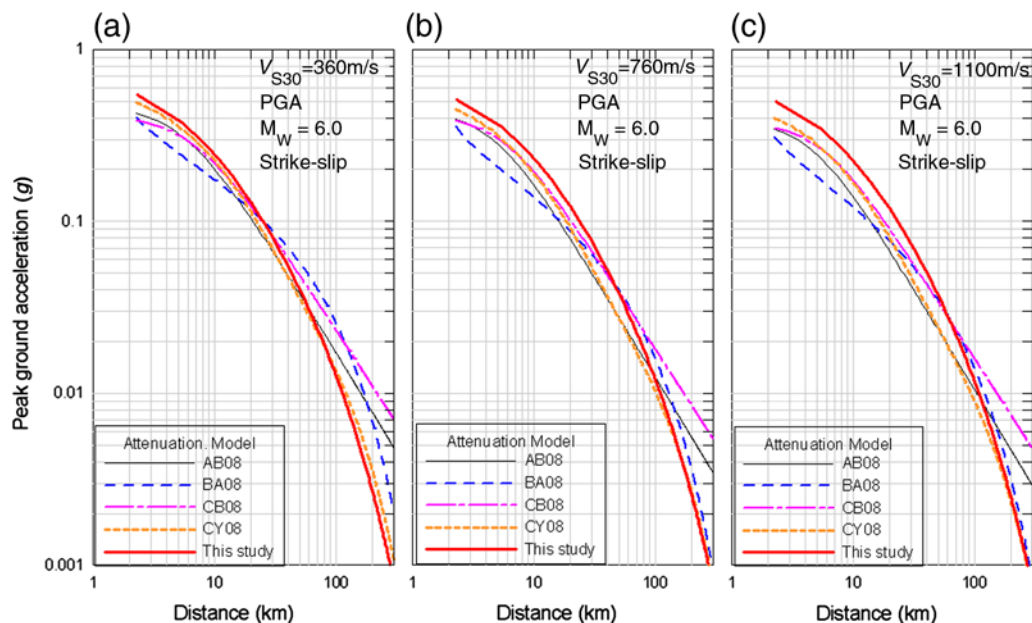


Figure 11. Plots of the mean attenuation relationships of the horizontal PGA as a function of distance for M_w 6 and strike-slip fault for the Ilan area and the four NGA models. (a–c) The cases with $V_{S30} = 360$ m/s, 760 m/s, and 1100 m/s respectively. The color version of this figure is available only in the electronic edition.

earthquakes, and nonspecified mechanism, respectively. Accordingly, we can find that all interevent residuals decrease with increasing magnitude faster in the strike-slip fault type than in the other two fault types for the vertical and horizontal components of PGA and PGV in the Ilan area.

In addition, the amplification factor of a fault type was calculated from the exponent of the interevent residual.

Figure 14a–d shows the fault-type factor as a function of magnitude in different fault types for the vertical and horizontal components of PGA and PGV in the Ilan area. The regression functions of different fault types are normalized by the regression function of all faults, which is represented by a solid line for which the fault-type factor is equal to one. From these figures, we can find the following results: (1) the

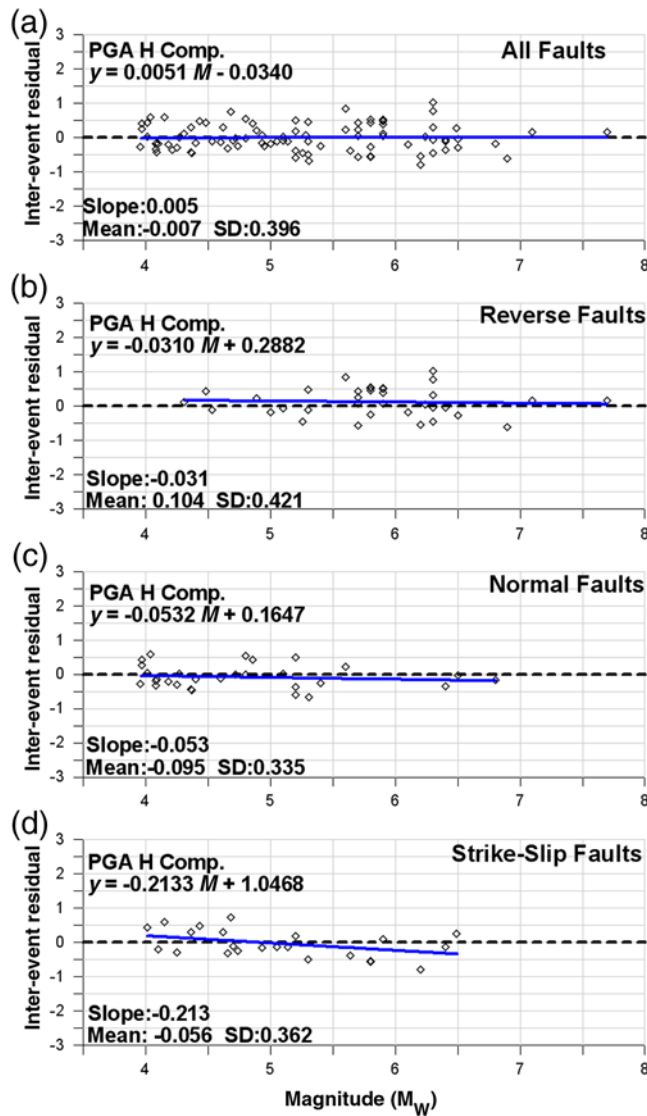


Figure 12. Plots of the interevent residuals as function of magnitude of different fault types for the horizontal components of PGA in the Ilan area. The dashed lines represent the baseline for residual equal to zero, while the solid lines represent the linear regression functions. The color version of this figure is available only in the electronic edition.

fault-type factor is not a constant, but is a function of magnitude for different fault types for the vertical and horizontal components of PGA and PGV; (2) the fault-type factor decreases with increasing magnitude faster in strike-slip fault type than in the other two fault types; (3) the reverse fault has the highest ground-motion amplification factor when the magnitude is greater than 4.4 among the three fault types, especially for the PGV; and (4), except in the horizontal component of PGV, the normal fault has a larger ground-motion amplification factor with magnitude greater than 5.2–5.6, as compared to that of the strike-slip fault.

A significant issue in performing attenuation model regression is that the regional differences in attenuation are known to exist (Boore, 1989; Boore and Atkinson, 2007).

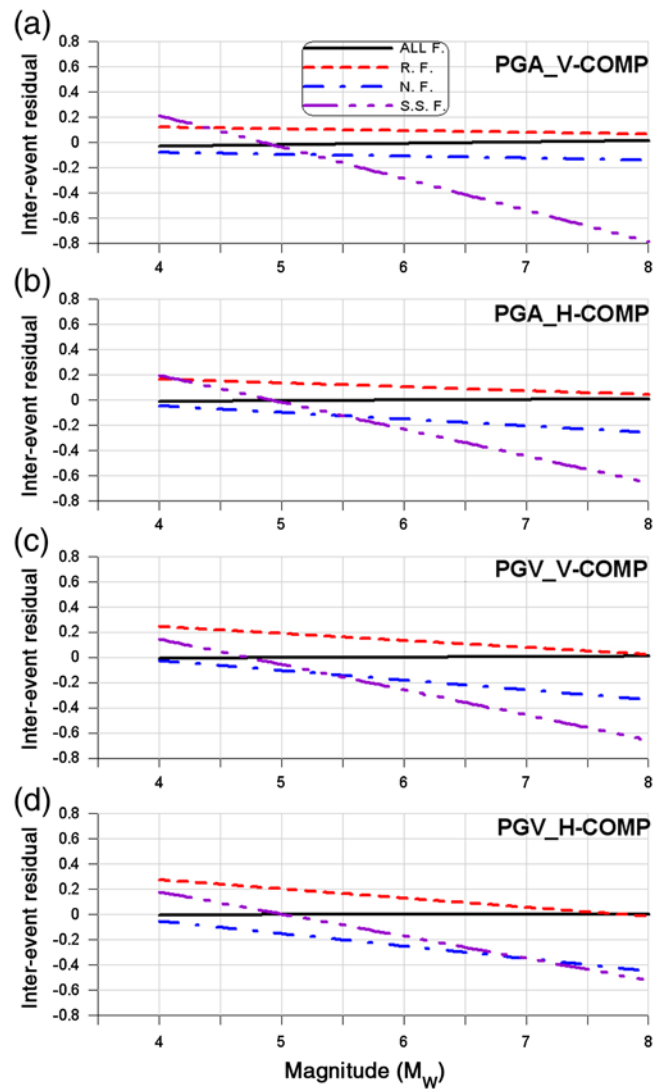


Figure 13. Plots of the interevent residuals as function of magnitude of different fault types for the vertical and horizontal components of PGA and PGV in the Ilan area. The color version of this figure is available only in the electronic edition.

The significance of regional effects can be tested by examining residual trends for subsets of data organized by source regions. In this study, the distribution of different types of earthquakes is uneven geographically.

In order to check whether the significant trend is caused by site effect, we tested the intraevent residuals obtained from the regression. Figures 15 and 16 show the intraevent residuals as a function of magnitude and distance, respectively, of different fault types for the horizontal components of PGA in the Ilan area. The dashed lines represent the baseline for residual equal to zero, while the solid lines represent the linear regression functions. In Figure 16, we find some high values in the < 60 km distance range, mostly contributed from ILA050, ILA065, and ILA066 in earthquakes of all three fault types. This is because these stations are all located on hard schist in the Nanao area (Ho, 1984). The high

Table 10
 Interevent Residuals of Different Fault Types for the Vertical and Horizontal Components of PGA and PGV

Number		Residuals	<i>a</i>	<i>b</i>	Sd	Residuals	<i>a</i>	<i>b</i>	Sd		
1	PGA	V-Comp.	R_{ALL}	0.0114	-0.0769	0.415	H-Comp.	R_{ALL}	0.0051	-0.0340	0.396
			R_{RS}	-0.0138	0.1764	0.424		R_{RS}	-0.0310	0.2882	0.421
			R_{NS}	-0.0150	-0.0196	0.364		R_{NS}	-0.0532	0.1647	0.335
			R_{SS}	-0.2504	1.2141	0.393		R_{SS}	-0.2133	1.0468	0.362
2	PGV	V-Comp.	R_{ALL}	0.0040	-0.0242	0.382	H-Comp.	R_{ALL}	0.0016	-0.0081	0.415
			R_{RS}	-0.0554	0.4649	0.428		R_{RS}	-0.0729	0.5686	0.467
			R_{NS}	-0.0774	0.2817	0.313		R_{NS}	-0.0988	0.3436	0.368
			R_{SS}	-0.2000	0.9423	0.280		R_{SS}	-0.1758	0.8844	0.277

$Res = aM + b \pm Sd$

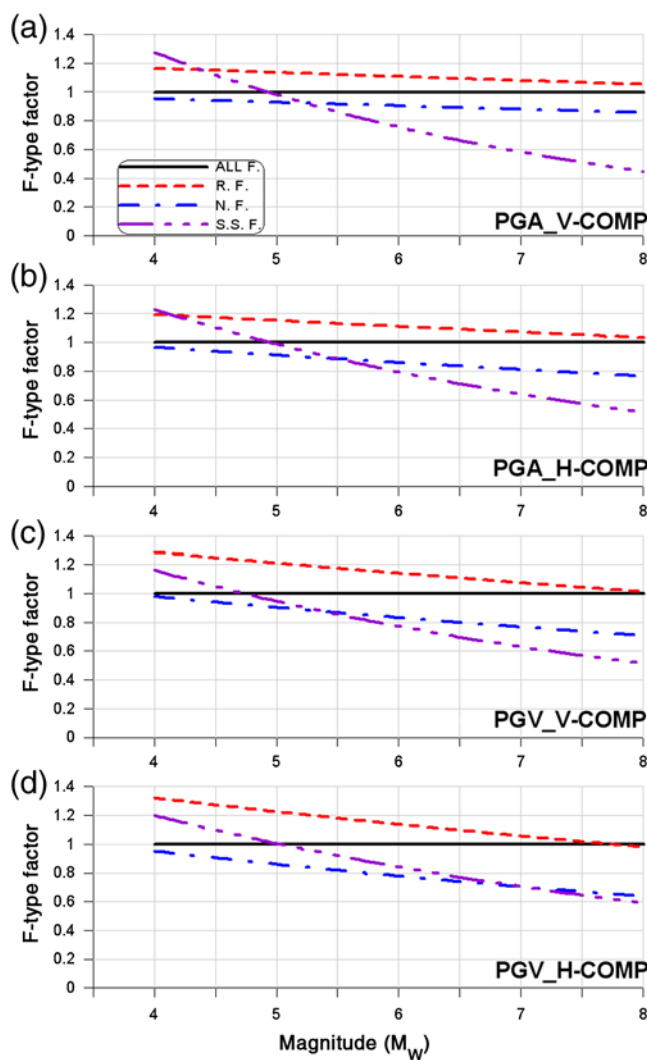


Figure 14. Plots of the fault-type factor as function of magnitude of different fault types for the vertical and horizontal components of PGA and PGV in the Ilan area. The regression functions of different fault type are normalized by the regression function of all faults, as represented by the solid line with a fault-type factor equal to one. The color version of this figure is available only in the electronic edition.

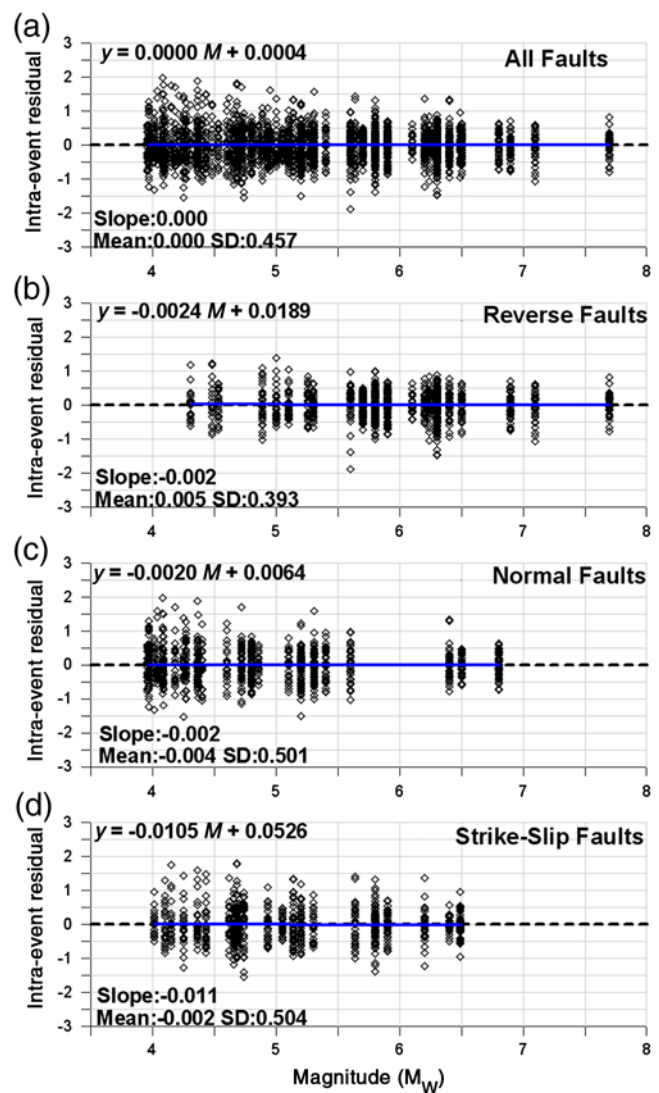


Figure 15. The intraevent residuals as function of magnitude of different fault types for the horizontal components of PGA in the Ilan area. The dashed lines represent the baseline for residual equal to zero, while the solid lines represent the linear regression functions. The color version of this figure is available only in the electronic edition.

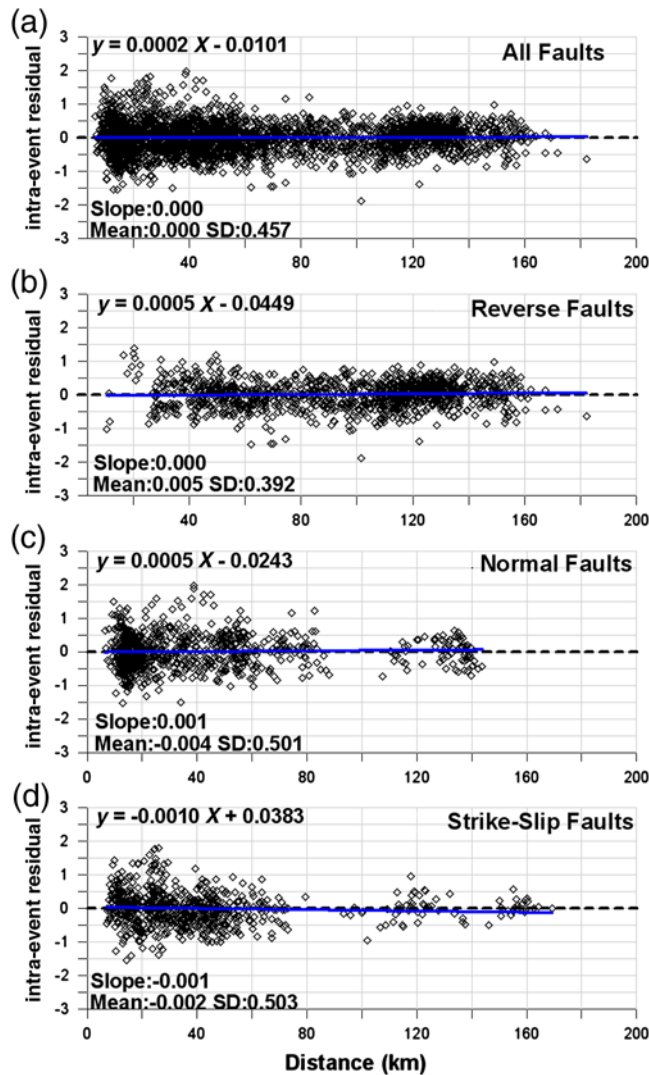


Figure 16. The intraevent residuals as function of distance of different fault types for horizontal PGA in the Ilan area. The dashed lines represent the baseline for residual equal to zero, while the solid lines represent the linear regression functions. The color version of this figure is available only in the electronic edition.

PGA residual anomaly of the Nanao area will be supported by later analyses for site residuals. Lack of significant trend of the intraevent residuals with magnitude and distance indicates that there is no bias attributable to site effect in our regression results.

In addition, in order to check whether the tendency of intraevent residuals depends on the path effect from the source to the target site, we test the intraevent residuals obtained in the three source areas of reverse earthquakes. The three areas (see Fig. 1) are the A area in the southwest direction of Ilan, including events 24, 25, 28, 30, 31, 32, 35, 36, and 92; the B area in the south direction of Ilan, including events 8, 11, 33, 38, 45, 48, 63, 64, 88, and 90; the C area in the southeast direction of Ilan, including events 2, 9, 12, 13, 18, 46, 51, 53, 55, 58, 61, 62, 81, 82, and 89, respectively.

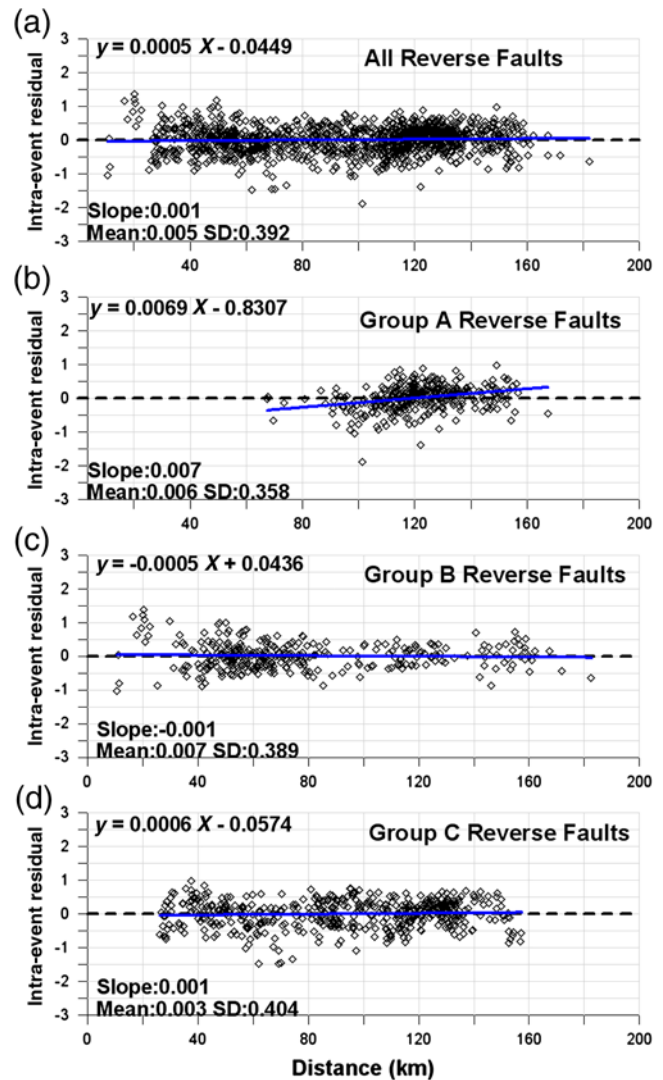


Figure 17. The intraevent residuals as function of distance for horizontal PGA for reverse earthquakes in whole and three sub-areas. The dashed lines represent the baseline for residual equal to zero, while the solid lines represent the linear regression functions. The color version of this figure is available only in the electronic edition.

The recording numbers for the three areas A, B, and C are 331, 324, and 503, respectively.

Figure 17 shows the intraevent residuals as a function of distance for the horizontal components of PGA for reverse earthquakes in total and three subareas. The dashed lines represent the baseline for residual equal to zero, while the solid lines represent the linear regression functions. From these figures, except the area A, we can find no trend of the intraevent residuals with distance for areas B and C. After checking the area A data, we found in Figure 17b higher clusters of data, at a distance of 110–130 km in southwestern areas, that probably represents moHo reflection due to paths crossing the Central Mountain Range (Liu and Tsai, 2009). The above results show that there is some bias in regression showing

Table 11

Intraevent and Total Residuals for the Vertical and Horizontal Components of PGA and PGV from Model 1

Number	Station	Latitude (° N)	Longitude (° E)	PGA _V _I	PGA _h _I	PGA _V _T	PGA _h _T	PGV _V _I	PGV _h _I	PGV _V _T	PGV _h _T
1	ILA001	24.883	121.835	-0.7603	-0.7784	-0.8066	-0.8176	-0.5784	-0.6485	-0.6244	-0.6961
2	ILA002	24.845	121.796	-0.1865	0.0723	-0.2676	0.0014	-0.078	0.2199	-0.1622	0.1226
3	ILA003	24.798	121.782	-0.2629	-0.0418	-0.3264	-0.0561	0.0071	0.2432	0.0047	0.2905
4	ILA004	24.745	121.782	-0.0812	0.004	-0.1634	-0.0508	0.1088	0.4005	0.0947	0.4168
5	ILA005	24.699	121.804	-0.1026	0.2353	-0.0339	0.3065	0.1094	0.3003	0.1615	0.3353
6	ILA006	24.641	121.824	0.032	0.1386	0.0762	0.187	0.1884	0.1837	0.2149	0.194
7	ILA007	24.594	121.845	0.3366	0.255	0.4291	0.3365	0.1275	0.076	0.1731	0.0858
8	ILA008	24.709	121.763	0.054	0.0167	0.0501	0.0251	0.023	0.0949	0.0308	0.1127
9	ILA010	24.619	121.781	0.0843	-0.1322	0.0946	-0.1148	-0.0174	-0.3626	-0.0153	-0.3547
10	ILA011	24.831	121.74	-0.0353	-0.397	-0.2167	-0.5247	-0.2353	-0.6147	-0.478	-0.7653
11	ILA012	24.781	121.734	-0.1977	-0.103	-0.183	-0.0632	-0.0596	0.099	-0.0331	0.1249
12	ILA013	24.735	121.729	-0.0748	0.333	-0.0417	0.3736	0.0607	0.3969	0.0848	0.4076
13	ILA014	24.695	121.719	-0.4409	0.0137	-0.4307	0.0513	-0.3716	-0.1164	-0.3587	-0.1186
14	ILA015	24.781	121.691	-0.2319	-0.4558	-0.3524	-0.5425	-0.3596	-0.5933	-0.435	-0.6504
15	ILA016	24.75	121.683	-0.1607	-0.1809	-0.1936	-0.1893	-0.1823	-0.0625	-0.1715	-0.0398
16	ILA017	24.722	121.68	-0.2799	-0.6027	-0.4455	-0.7452	-0.0564	-0.3236	-0.1157	-0.3429
17	ILA018	24.682	121.68	-0.4049	-0.3863	-0.497	-0.4572	-0.4398	-0.4147	-0.4587	-0.3914
18	ILA019	24.644	121.693	-0.1667	-0.3073	-0.1557	-0.3257	-0.1724	-0.4361	-0.194	-0.5055
19	ILA020	24.756	121.627	-0.2437	-0.2385	-0.3593	-0.3128	-0.1889	-0.3765	-0.2201	-0.3441
20	ILA021	24.713	121.645	-0.3312	-0.5242	-0.4081	-0.561	-0.3527	-0.5686	-0.3694	-0.5556
21	ILA022	24.669	121.643	-0.0786	-0.6423	-0.1729	-0.776	-0.1375	-0.5524	-0.2352	-0.6542
22	ILA023	24.684	121.599	0.0369	-0.258	-0.015	-0.3101	-0.1897	-0.4035	-0.2052	-0.4089
23	ILA024	24.662	121.611	-0.5206	-0.7269	-0.5711	-0.7744	-0.5646	-0.9804	-0.6319	-1.0465
24	ILA025	24.638	121.563	-0.1468	0.2551	-0.1869	0.2172	-0.2165	-0.213	-0.2446	-0.2444
25	ILA026	24.675	121.765	0.2114	0.1511	0.2659	0.1919	0.3045	0.266	0.3441	0.2793
26	ILA027	24.691	121.759	-0.1289	-0.0091	-0.239	-0.11	0.0143	0.3062	-0.0406	0.2578
27	ILA028	24.756	121.747	0.2952	0.2075	0.284	0.1928	0.35	0.4326	0.3593	0.4557
28	ILA029	24.773	121.746	0.0247	-0.2455	-0.1273	-0.3945	0.1897	0.1716	0.1285	0.1556
29	ILA030	24.728	121.756	0.0223	0.0592	-0.014	0.0634	0.1239	0.4052	0.1503	0.4783
30	ILA031	24.599	121.832	0.3826	0.3269	0.3735	0.3187	0.029	-0.1392	0.0159	-0.1578
31	ILA032	24.623	121.828	-0.3715	-0.0301	-0.4178	-0.0582	0.0161	0.1095	-0.0035	0.1083
32	ILA033	24.864	121.82	-0.0251	-0.078	-0.1621	-0.2609	-0.1346	-0.134	-0.3049	-0.3318
33	ILA034	24.804	121.806	0.2104	-0.2244	0.0905	-0.3153	0.225	0.1197	0.1951	0.1447
34	ILA035	24.824	121.76	-0.553	-0.2949	-0.5945	-0.3336	-0.104	0.0633	-0.0833	0.1086
35	ILA036	24.789	121.752	-0.2339	-0.2014	-0.2735	-0.1982	-0.1075	0.0684	-0.0854	0.1296
36	ILA037	24.745	121.715	0.2124	0.0714	0.1944	0.0679	0.1913	0.206	0.1839	0.2091
37	ILA038	24.721	121.735	-0.3713	-0.0647	-0.4355	-0.1148	-0.038	0.2211	-0.0392	0.2478
38	ILA039	24.766	121.722	-0.1249	-0.1971	-0.1915	-0.2649	0.2754	0.3761	0.2327	0.3141
39	ILA040	24.774	121.791	0.0765	0.2	0.1992	0.3208	0.1996	0.5612	0.3406	0.7239
40	ILA041	24.724	121.792	-0.0529	0.1493	-0.0466	0.1817	-0.0408	0.3828	-0.0009	0.4425
41	ILA042	24.689	121.79	-0.1273	0.0491	-0.1472	0.0358	-0.1288	0.1828	-0.1301	0.1852
42	ILA043	24.629	121.735	-0.0161	-0.1621	-0.0315	-0.1744	0.2223	-0.2329	0.2134	-0.2567
43	ILA044	24.656	121.755	0.3307	-0.0541	0.3255	-0.0444	0.4924	0.1549	0.5182	0.1867
44	ILA046	24.667	121.734	-0.1324	-0.2482	-0.1782	-0.2722	-0.2159	-0.3225	-0.2427	-0.3421
45	ILA047	24.645	121.786	-0.0931	0.0606	-0.1353	0.0127	-0.145	0.145	-0.1443	0.168
46	ILA048	24.767	121.762	-0.0538	0.2703	-0.114	0.2581	0.1766	0.4338	0.1879	0.4856
47	ILA049	24.766	121.748	-0.1623	-0.1258	-0.2341	-0.1606	-0.0118	0.1366	-0.0351	0.1429
48	ILA050	24.428	121.74	0.368	0.803	0.362	0.7927	-0.072	0.0415	-0.1233	-0.0238
49	ILA051	24.72	121.675	-0.2451	-0.3064	-0.3054	-0.3435	-0.2743	-0.3524	-0.29	-0.3449
50	ILA052	24.61	121.851	-0.4592	-0.3927	-0.4722	-0.3955	-0.4448	-0.6442	-0.4811	-0.6699
51	ILA053	24.331	121.731	0.1897	-0.2114	0.2262	-0.2008	0.128	-0.324	0.1272	-0.3514
52	ILA054	24.972	121.918	-0.5945	-0.4303	-0.6368	-0.4197	-0.554	-0.4987	-0.6655	-0.5891
53	ILA055	24.738	121.809	0.1025	0.1628	0.1316	0.1823	0.1176	0.2468	0.1181	0.2183
54	ILA056	24.761	121.808	-0.2142	0.0753	-0.1885	0.1275	0.1086	0.4003	0.1606	0.4523
55	ILA057	24.807	121.741	-0.4949	-0.6471	-0.6189	-0.7835	-0.2741	-0.6703	-0.3534	-0.6929
56	ILA058	24.677	121.75	0.1682	0.1666	0.1935	0.1949	0.076	0.1625	0.1195	0.2157
57	ILA059	24.667	121.821	0.1702	0.0663	0.2063	0.1126	0.1626	0.1039	0.1909	0.1065
58	ILA060	24.578	121.836	0.4635	0.1029	0.4912	0.1119	0.1067	-0.3483	0.1201	-0.3395
59	ILA061	24.523	121.825	0.0907	-0.2568	0.1481	-0.2117	-0.203	-0.4662	-0.1774	-0.4723
60	ILA062	24.468	121.792	0.4905	0.2301	0.5299	0.2531	0.2178	0.006	0.2071	-0.0512
61	ILA063	24.49	121.419	-0.1785	-0.2483	-0.1838	-0.2337	-0.313	-0.7248	-0.2997	-0.7004

(continued)

Table 11 (Continued)

Number	Station	Latitude (° N)	Longitude (° E)	PGA _{v_i}	PGA _{h_i}	PGA _{v_T}	PGA _{h_T}	PGV _{v_i}	PGV _{h_i}	PGV _{v_T}	PGV _{h_T}
62	ILA064	24.478	121.777	0.3542	0.0105	0.3972	0.0274	0.0024	-0.3017	0.0038	-0.3536
63	ILA065	24.473	121.769	0.7262	0.4416	0.8272	0.4989	0.3595	-0.0245	0.394	-0.032
64	ILA066	24.447	121.77	0.4499	0.3157	0.472	0.3321	0.0999	-0.0392	0.107	-0.0461
65	ILA067	24.439	121.373	-0.3492	-0.0685	-0.3189	-0.022	-0.2863	-0.1999	-0.281	-0.1901

PGA_{v_i}, PGA_{h_i}: Intraevent residual for the vertical and horizontal components of peak ground acceleration (PGA), respectively.
 PGA_{v_T}, PGA_{h_T}: Total residual for the vertical and horizontal components of peak ground acceleration (PGA), respectively.
 PGV_{v_i}, PGV_{h_i}: Intraevent residual for the vertical and horizontal components of peak ground velocity (PGV), respectively.
 PGV_{v_T}, PGV_{h_T}: Total residual for the vertical and horizontal components of peak ground velocity (PGV), respectively.

path effect when earthquakes occur to the west of the Central Mountain Range.

Site Residuals in Model 1

Examination of the residuals for sites with different soil categories is a useful method for sets of records where site information is not complete (Abrahamson and Litehiser, 1989). In this study, we first analyzed the residuals to investigate variations of PGA and PGV with respect to site conditions. We denote the total residual as the site-response factor and the intraevent residual as the site-amplification factor, respectively. The site-response factor includes both source and site effects relative to the recording station, whereas the site-amplification factor only includes site effects. The site total and intraevent residuals for the vertical and horizontal PGA and PGV are given in Table 11. The contour maps of site total and intraevent residuals for horizontal PGA and PGV are shown in Figures 18–21, respectively. The triangle-shaped

thick lines in the maps represent the outline of Ilan Plain. Residual contours are shown at 0.1 intervals.

These results show that the logarithmic horizontal PGA site total and intraevent residuals range from 0.79 to -0.82 and 0.80 to -0.78, respectively, corresponding to amplification factors ranging from 2.20 to 0.44 and 2.23 to 0.46. As mentioned earlier, the high PGA residual anomalies in the Nanao area can be attributed to hard schist rocks (Ho, 1984). In addition, the logarithmic horizontal PGV site total and intraevent residuals range from 0.72 to -1.05 and 0.56 to -0.98, respectively, corresponding to amplification factors ranging from 2.05 to 0.35 and 1.75 to 0.38. The contour maps of site-total and intraevent residuals of horizontal PGV have similar patterns. They all reveal that the Zhuangwei Township, Ilan City, and Luodong Township have high residual values indicating significant amplification of ground motions. In contrast, the surrounding regions such as Sanxing Township and Datong Township have negative residual values.

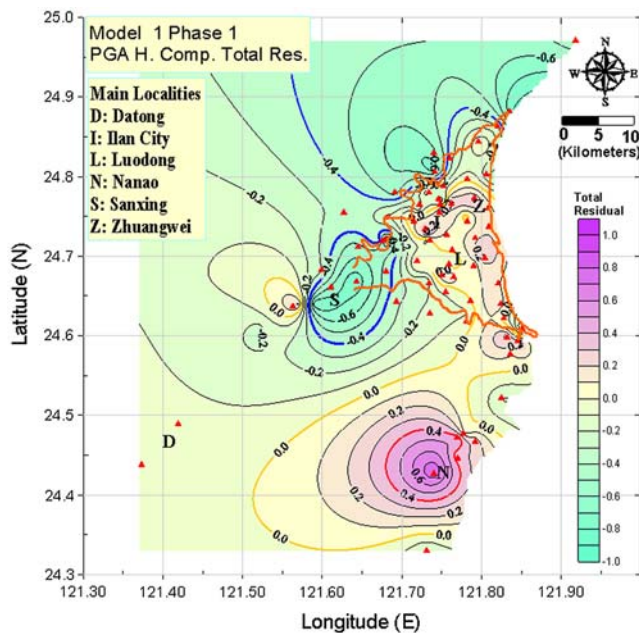


Figure 18. Distribution of the total residual values (difference between logarithms of observed and predicted accelerations) for horizontal PGA. The triangle-shaped thick line in the map marks the outline of Ilan Plain. Main localities are also indicated. The color version of this figure is available only in the electronic edition.

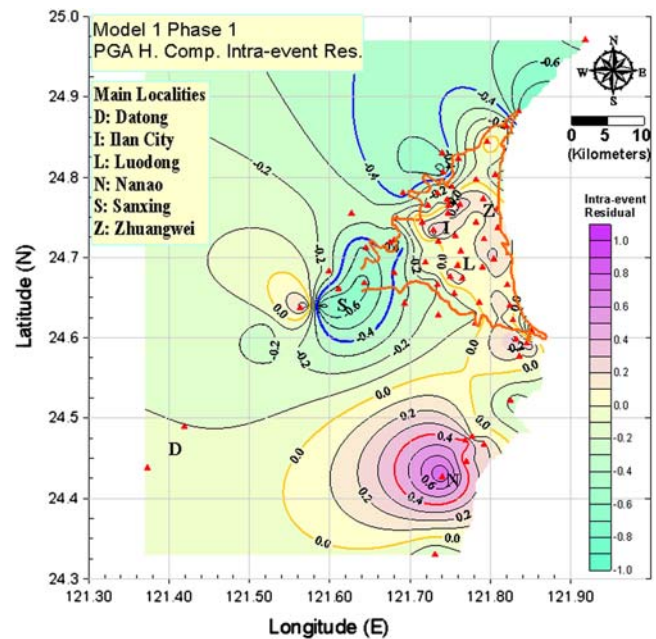


Figure 19. Distribution of the horizontal PGA intraevent residual values (difference between logarithms of observed and predicted accelerations). The triangle-shaped thick line in the map marks the outline of Ilan Plain. Main localities are also indicated. The color version of this figure is available only in the electronic edition.

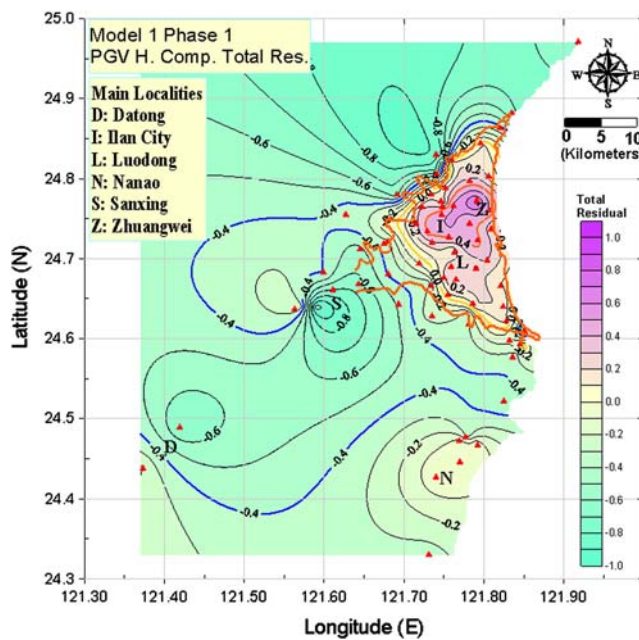


Figure 20. Distribution of the total residual values (difference between logarithms of observed and predicted accelerations) for horizontal PGV. The triangle-shaped thick line in the map marks the outline of Ilan Plain. Main localities are also indicated. The color version of this figure is available only in the electronic edition.

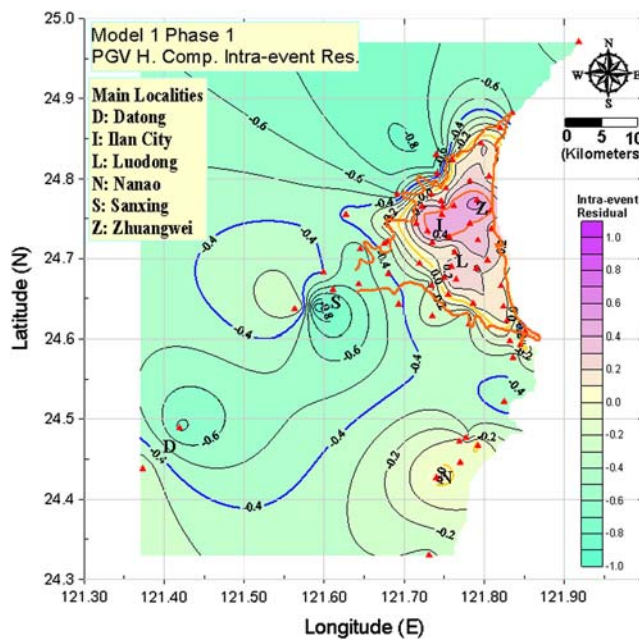


Figure 21. Distribution of the intraevent residual values (difference between logarithms of observed and predicted accelerations) for horizontal PGV. The triangle-shaped thick line in the map marks the outline of Ilan Plain. Main localities are also indicated. The color version of this figure is available only in the electronic edition.

The Ilan Plain is an alluvial delta located at the north-eastern coast, opening to the Okinawa trough toward the east. The two other sides are fringed by high mountains composed mainly of Miocene to Paleogene slates (Ho, 1982).

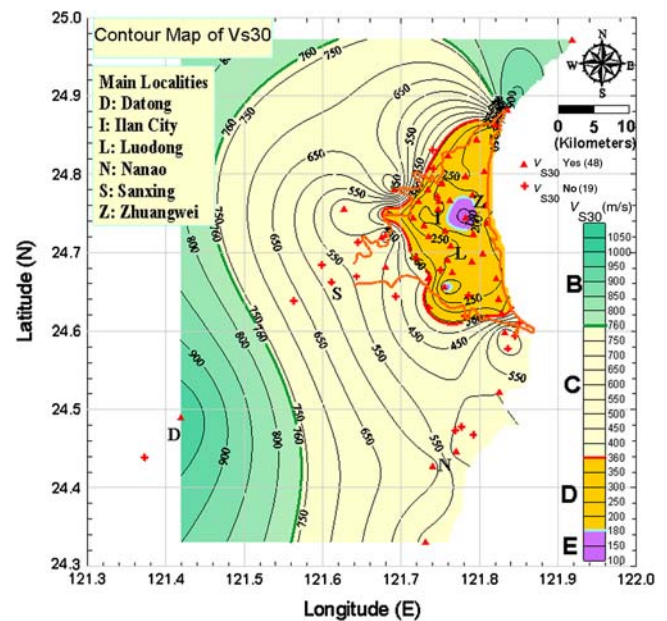


Figure 22. Distribution of V_{S30} (the average shear-wave velocity over the top 30 m) in the Ilan area. The triangle-shaped thick line in the map marks the outline of Ilan Plain. Main localities are also indicated. The color version of this figure is available only in the electronic edition.

The results of past seismic experiments in Ilan Plain, such as a reflection (Chiang, 1976) and a refraction survey (Wen and Yeh, 1984) demonstrate that the plain has thick sediments with low S -wave velocities of 120–850 m/s, and that the basement tilts downward to the northeast. The depth of the basement is about 1400 m at the center of the basin (Furumura *et al.*, 2001). The site residual patterns, especially those for PGV, can be clearly correlated with the basement depth. These results agree reasonably well with regional geology and topography.

Moreover, the PGV residuals are found to be more sensitive to the site effect than the PGA residuals, because PGA is primarily a high-frequency ground-motion parameter, which is less affected by local site conditions. Local site conditions can drastically affect the recorded strong motions (Douglas, 2003). PGA and PGV are often useful for analysis of short-period ($T < 0.3$ s) and intermediate-period ($T = 0.3 \sim 1$ s) structures (Liu, 1999).

Furthermore, in order to understand the relation between the site residuals of ground-motion parameters and V_{S30} , we plot the V_{S30} contours as shown in Figure 22. V_{S30} contours are shown at 50 m/s intervals. We also found that the PGV residual contour patterns are very similar to the V_{S30} contour patterns. Both relations are discussed below.

Site Residuals in Model 2 (Including V_{S30})

Finally, we display the average intraevent residual contour map for horizontal PGV from equation (5) and in Figure 23. Residual contours are shown at 0.1 intervals and the intraevent residual results show that the logarithmic

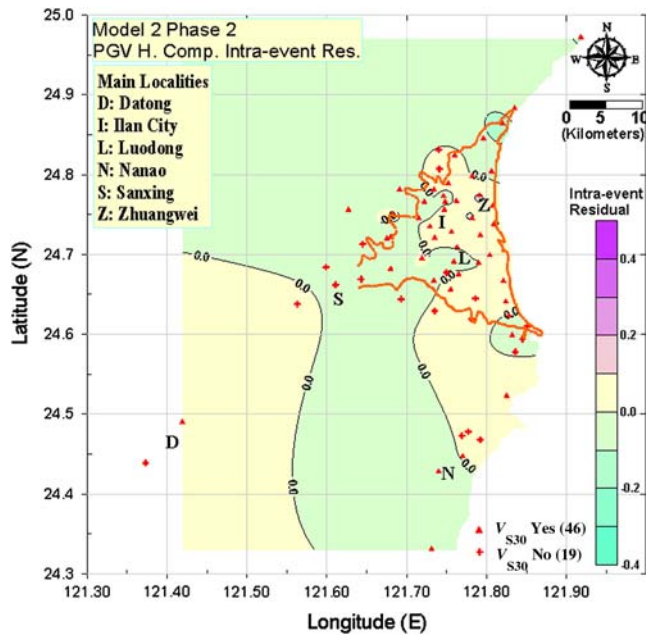


Figure 23. The site intraevent residual contour map for horizontal PGV. The triangle-shaped thick line in the map marks the outline of Ilan Plain. Main localities are also indicated. The color version of this figure is available only in the electronic edition.

PGV site residuals range from -0.1 to 0.1 . From Figures 21 and 23, we can identify the effectiveness of the V_{S30} correction, which reduces site specific residuals in PGV.

Furthermore, we analyzed the site-effect term by using the amplification factor (relative to a site with $V_{S30} = 760$ m/s) $\exp[c6 \times \ln(V_{S30}/760) + Res_{av}]$, where Res_{av} is the average intraevent residual from equation (5) for each site. We use the values from the final model to ensure that any effects that were not modeled will be eliminated. In this study, we specify V_{ref} as the reference velocity of 760 m/s. Thus, the soil amplifications are specified relative to motions that would be recorded on a B/C boundary site condition.

The corrected site-amplification factor contour map relative to a B/C boundary site condition for the horizontal PGV is plotted in Figure 24. The amplification-factor contours are shown at 0.1 intervals and range from 2.82 to 0.73. The site total, intraevent residual, and amplification factors residual contour maps of horizontal PGV all have similar patterns, revealing that the Zhuangwei Township, Ilan City, and Luodong Township have high values, implying large amplification of ground motions.

By comparing the contour maps in Figures 20, 21, and 24, we can make the following statements:

1. The three site contour patterns are similar, especially for the residual values corresponding to 0 in Figures 20 and 21 and amplification factors corresponding to 1.6 in Figure 24, even though some parts of the contours are generated based on few stations. Fortunately, these parts are mostly located outside the Ilan plain. In general, geomorphology and geology may also play an important

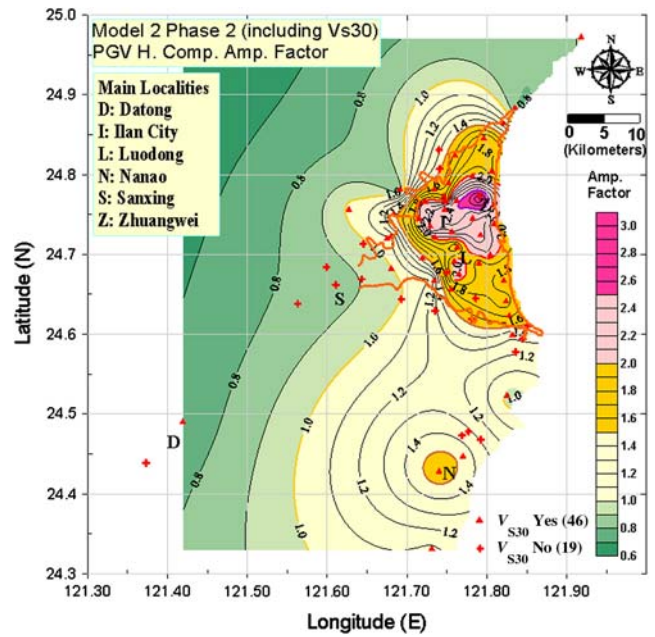


Figure 24. The corrected site-amplification factor contour map with respect to the B/C boundary site conditions for horizontal PGV. The triangle-shaped thick line in the map marks the outline of Ilan Plain. Main localities are also indicated. The color version of this figure is available only in the electronic edition.

role in site effect. The residual lines of 0 in Figures 20 and 21 and amplification factor of 1.6 in Figure 24 tend to coincide with an elevation of 10 m and a sediment depth of 200 m.

2. Figures 20 and 21 represent the site-response factor by the total residual, and the site-amplification factor by the intraevent residual, respectively. The site-response factor includes both source and site effects relative to the recording station, whereas the site-amplification factor only includes the site effect. Both site contour maps are calculated by using residuals at all 65 Ilan stations.
3. In contrast, Figure 24 represents the site-effect term relative to a site with $V_{S30} = 760$ m/s. The values are calculated by using the 46 strong-motion sites in Ilan area that have measurements of V_{S30} .
4. Following a disastrous earthquake, rapid assessment and timely reporting of the PGA and PGV maps will be critical for effective emergency-response operations. Thus, after an earthquake, we can combine these simple attenuation relationships, as determined from equation (2) and the site-response factors (total residuals), as determined from Figures 18 and 20 and Table 11 to provide near-real-time estimation and reporting of the PGA and PGV values throughout the Ilan area.

Conclusions

In this study, two models of attenuation relationship are used to account for different situations. Model 1, by using all

65 strong-motion sites, will be especially useful for the early warning system to quickly produce and report the PGA and PGV maps for effective emergency-response operations. On the other hand, Model 2, by using the 46 strong-motion sites to incorporate a site-effect term, V_{S30} , is aimed at reducing the standard deviation of the predicted ground motion for engineering purposes. Based on above results, we can summarize as follows:

1. The attenuation relationships for PGA indicate faster decay with distance for the vertical component than for the horizontal component in the Ilan area. Furthermore, the attenuation relationships of PGA decay faster with distance than those of PGV for both the vertical and horizontal components.
2. From the variations of residuals related to fault type, we found that the fault-type amplification factor is not a constant, but varies as a function of magnitude for different fault types. The factor decreases with increasing magnitude faster for the strike-slip fault type than the reverse or normal fault types. The reverse fault has the highest ground-motion amplification factor among the three fault types when the magnitude is greater than 4.4, especially for the PGV. Furthermore, except in the horizontal component of PGV, the normal fault has a larger ground-motion amplification factor than that of the strike-slip fault for magnitudes greater than 5.2–5.6.
3. From the intraevent residuals as a function of distance for the horizontal component of PGA for reverse earthquakes, we found clusters of higher-value data at a distance of 110–130 km in southwestern areas (Area A data). They were probably caused by moho reflection with propagation paths crossing the Central Mountain Range. The results indicate some bias in regression showing path effects from earthquakes occurred to the west of the Central Mountain Range.
4. The ground-motion residual maps, especially for the PGV, show highly positive correlation with regional geology and topography of the Ilan area. The PGV residual contours reveal that Zhuangwei Township, Ilan City, and Luodong Township have high residual values that call for special attention in seismic design of structures.
5. The PGV residual contour patterns are similar to those of the V_{S30} contours. It is also found that the PGV residual is more closely correlated with the V_{S30} than the PGA residual, since the PGA is primarily a high-frequency parameter, which is not a simple function of V_{S30} .
6. Comparing the standard deviations of the residuals between the observed and predicted values before and after incorporating the fault-type and site-effect term of V_{S30} , the change of standard deviation for PGA is 2.3%. In contrast, the PGV standard deviation was significantly reduced by 11.6%. Obviously, the attenuation relationship in Model 2 can serve more appropriately for engineering purposes, especially for PGV.

7. Finally, following a disastrous earthquake, quick assessment and timely reporting of PGA and PGV maps will be critical for effective emergency-response operations. Thus, after an earthquake, we can combine the simple attenuation relationships, as determined from equation (2), and the site-response factor (total residuals), as determined from Table 11, to provide near-real-time estimation and reporting of the PGA and PGV values for the Ilan area.

Data and Resources

Seismograms used in this study were collected by 16-bit accelerographs installed as part of the Taiwan Strong-Motion Instrumentation Program (TSMIP). The digital TSMIP strong-motion data can be obtained from the Central Weather Bureau of Taiwan at <http://www.cwb.gov.tw> by going to http://www.cwb.gov.tw/V7e/about/Data_Application.htm (last accessed November 2012).

Acknowledgments

We thank the Central Weather Bureau of Taiwan for providing us with the strong-motion data. We are grateful to Hiroshi Kawase and anonymous reviewers for their critical and helpful comments, which have led to significant improvement of the paper. The focal mechanism data provided by Easy Chen, and Figure 1 adapted with permission from TAO are also greatly appreciated. This research was supported by the Taiwan Earthquake Research Center (TEC) funded through the National Science Council (NSC) with Grant Number NSC101-2116-M-244-001. The TEC Contribution Number for this article is 00091.

References

- Abrahamson, N. A., and J. J. Litehiser (1989). Attenuation of vertical peak acceleration, *Bull. Seismol. Soc. Am.* **79**, 549–580.
- Abrahamson, N. A., and W. Silva (2008). Summary of the Abrahamson & Silva NGA ground-motion relations, *Earthq. Spectra* **24**, 67–97.
- Abrahamson, N., G. Atkinson, D. Boore, Y. Bozognia, K. Campbell, B. Chiou, I. M. Idriss, W. Silva, and R. Youngs (2008). Comparisons of the NGA ground-motion relations, *Earthq. Spectra* **24**, 45–66.
- Akaike, H. (1974). A new look at the statistical model identification, *IEEE Trans. Automat. Contr.* **19**, 716–723.
- Aki, K., and P. G. Richards (1980). *Quantitative Seismology Theory and Methods*, Vol. 1, W. H. Freeman, 557 pp.
- Bolt, B. A., and N. A. Abrahamson (2004). Estimation of strong seismic ground motion, in *International Handbook of Earthquake and Engineering Seismology*, W. Lee (Editor), Academic Press, 983–1001.
- Boore, D. M. (1989). The Richter scale: Its development and use for determining earthquake source parameters, *Tectonophysics* **166**, 1–14.
- Boore, D. M. (2005). Erratum: Equations for estimating horizontal response spectra and peak acceleration from western North American earthquakes: A summary of recent work, *Seismol. Res. Lett.* **76**, 368–369.
- Boore, D. M., and G. M. Atkinson (2006). Boore–Atkinson NGA empirical ground motion model for the average horizontal component of PGA, PGV and SA at spectral periods of 0.1, 0.2, 1, 2, and 3 seconds, *PEER Interim Report 2006/07*, Pacific Earthquake Engineering Center, Berkeley, California.
- Boore, D. M., and G. M. Atkinson (2007). Boore–Atkinson NGA ground motion relations for the geometric mean horizontal component of peak and spectral ground motion parameters, *PEER Report 2007/01*, Pacific Earthquake Engineering Center, Berkeley, California.
- Boore, D. M., and G. M. Atkinson (2008). Ground-motion prediction equations for the average horizontal component of PGA, PGV, and

- 5%-damped PSA at spectral periods between 0.01 s and 10.0 s, *Earthq. Spectra* **24**, 99–138.
- Boore, D. M., W. B. Joyner, and T. E. Fumal (1993). Estimation of response spectra and peak accelerations from western North American earthquakes: An interim report, *U.S. Geol. Surv. Open-File Rept. 93-509*, 70 pp.
- Boore, D. M., W. B. Joyner, and T. E. Fumal (1997). Equations for estimating horizontal response spectra and peak acceleration from western North American earthquakes—A summary of recent work, *Seismol. Res. Lett.* **68**, 128–153.
- Campbell, K. W. (1997). Empirical near-source attenuation relationships for horizontal and vertical components of peak ground acceleration, peak ground velocity, and pseudo-absolute acceleration response spectra, *Seismol. Res. Lett.* **68**, no. 1, 154–179.
- Campbell, K. W. (2004). Strong-motion attenuation relations, in *International Handbook of Earthquake and Engineering Seismology*, W. Lee (Editor), Academic Press, 1003–1012.
- Campbell, K. W., and Y. Bozorgnia (2006). Campbell–Bozorgnia NGA Empirical Ground Motion Model for the Average Horizontal Component of PGA, PGV and SA at Selected Spectral Periods Ranging from 0.01–10.0 Seconds, *Interim Report for USGS Review*, 87 pp.
- Campbell, K. W., and Y. Bozorgnia (2007). Campbell–Bozorgnia NGA Ground Motion Relations for the Geometric Mean Horizontal Component of Peak and Spectral Ground Motion Parameters, *Report PEER 2007/02*, Pacific Earthquake Engineering Research Center.
- Campbell, K. W., and Y. Bozorgnia (2008). NGA ground motion model for the geometric mean horizontal component of PGA, PGV, PGD and 5% damped linear elastic response spectra for periods ranging from 0.01 to 10 s, *Earthq. Spectra* **24**, 139–171.
- Chen, K. P., and Y. B. Tsai (2008). A catalog of Taiwan earthquake with homogenized M_w magnitude from 1900 to 2006, *Bull. Seismol. Soc. Am.* **98**, 483–489.
- Chiang, S. C. (1976). A seismic refraction prospecting of the Ilan plain (in Chinese), *Mining Tech.* **14**, 215–221.
- Chiou, B. S.-J., and R. R. Youngs (2006). Chiou and Youngs PEER–NGA empirical ground motion model for the average horizontal component of peak acceleration and pseudo-spectral acceleration for spectral periods of 0.01–10 seconds, *Interim Report for U.S. Geol. Surv. Rev.*, 71 pp.
- Chiou, B. S., and R. R. Youngs (2008). An NGA model for the average horizontal component of peak ground motion and response spectra, *Earthq. Spectra* **24**, 173–215.
- Douglas, J. (2003). Earthquake ground motion estimation using strong-motion records: A review of equations for the estimation of peak ground acceleration and response spectral ordinates, *Earth Sci. Rev.* **61**, 43–104.
- Douglas, J. (2011). Ground-motion prediction equations 1964–2010, *PEER Report PEER 2011/102*, Pacific Earthquake Engineering Research Center.
- Furumura, M., T. Furumura, and K. L. Wen (2001). Numerical simulation of love wave generation in the Ilan Basin, Taiwan, during the 1999 Chi-Chi earthquake, *Geophys. Res. Lett.* **28**, no. 17, 3385–3388.
- Hanks, T. C., and H. Kanamori (1979). A moment magnitude scale, *J. Geophys. Res.* **84**, 2348–2350.
- Heaton, T. F., F. Tajima, and A. W. Mori (1986). Estimating ground motions using recorded accelerogram, *Surv. Geophys.* **8**, 25–83.
- Ho, C. S. (1982). *Tectonic Evolution of Taiwan, Explanatory Text of the Tectonic Map of Taiwan*, Central Geologic Survey, The Ministry of economic Affairs, Taiwan, R.O.C.
- Ho, C. S. (1984). *An Introduction to the Geology of Taiwan, Explanatory Text of the Geology Map of Taiwan*, Second Ed., Central Geologic Survey, The Ministry of economic Affairs, Taiwan, R.O.C.
- Joyner, W. B., and D. M. Boore (1993). Method for regression analysis of strong-motion data, *Bull. Seismol. Soc. Am.* **83**, 469–487.
- Kao, H. (1998). Can great earthquakes occur in the southernmost Ryukyu arc–Taiwan region? *TAO* **9**, no. 3, 487–508.
- Kao, H., and R.-J. Rau (1999). Detailed structures of the subducted Philippine Sea plate beneath northeast Taiwan: A new type of double seismic zone, *J. Geophys. Res.* **104**, 1015–1033.
- Lee, C. T., C. T. Cheng, C. W. Liao, and Y. B. Tsai (2001). Site classification of Taiwan free-field strong motion stations, *Bull. Seismol. Soc. Am.* **91**, 1283–1297.
- Liu, K. S. (1999). Attenuation relations for strong seismic ground motion in Taiwan, *Ph. D. Thesis*, National Central University, Chungli, Taiwan, 240 pp. (in Chinese with English abstract).
- Liu, K. S., and Y. B. Tsai (2005). Attenuation relationships of peak ground acceleration and velocity for crustal earthquakes in Taiwan, *Bull. Seismol. Soc. Am.* **95**, 1045–1058.
- Liu, K. S., and Y. B. Tsai (2009). Large effects of Moho reflections (SmS) on peak ground motion in northwestern Taiwan, *Bull. Seismol. Soc. Am.* **99**, 255–267.
- Liu, K. S., T. C. Shin, and Y. B. Tsai (1999). A free-field strong-motion network in Taiwan: TSMIP, *TAO* **10**, no. 2, 377–396.
- Pinheiro, J., D. Bates, S. DebRoy, D. Sarkar, and The R Core Team (2011). nlme: Linear and nonlinear mixed effects models, *R package version 3.1-102*.
- Power, M., B. Chiou, N. Abrahamson, Y. Bozorgnia, T. Shantz, and C. Roblee (2008). An overview of the NGA project, *Earthq. Spectra* **24**, no. 1, 3–21.
- Rau, R.-J., and F. T. Wu (1998). Active tectonics of Taiwan orogeny from focal mechanisms of small-to-moderate-sized earthquakes, *TAO* **9**, no. 4, 755–778.
- Reiter, L. (1991). *Earthquake Hazard Analysis: Issues and Insights*, Columbia University Press, New York, 254 pp.
- Sadigh, K., C. Y. Chang, J. A. Egan, F. Makdisi, and R. R. Youngs (1997). Attenuation relationships for shallow crustal earthquake based on California strong motion data, *Seismol. Res. Lett.* **68**, no. 1, 180–189.
- Somerville, P. G., and N. Abrahamson (1995). Ground-motion prediction for thrust earthquakes, *Proc. SMIP95 Seminar*, Calif. Div. of Mines and Geology, San Francisco, California, 11–23.
- Spudich, P., J. Fletcher, M. Hellweg, J. Boatwright, C. Sullivan, W. Joyner, T. Hanks, D. Boore, A. McGarr, L. Baker, and A. Lindh (1996). Earthquake ground motions in extensional tectonic regimes, *U.S. Geol. Surv. Open-File Rept. 96-292*, 351 pp.
- Wen, K. L., and Y. T. Yeh (1984). Seismic velocity structure beneath the SMART1 array, *Bull. Inst. Earth Sci. Acad. Sin.* **4**, 51–72.
- Youngs, R. R., S.-J. Chiou, W. J. Silva, and J. R. Humphrey (1997). Strong ground motion attenuation relationships for subduction zone earthquakes, *Seismol. Res. Lett.* **68**, no. 1, 58–73.
- Department of Civil Engineering & Hazard Mitigation Research Center
Kao Yuan University
1821 Chung-Shan Rd, Lu-Chu Dist.
Kaohsiung City 82151, Taiwan R.O.C.
lk.sung99@msa.hinet.net
(K.-S.L.)
- 481 Patrick Way
Los Altos, California 94022
tsai_b@yahoo.com
(Y.-B.T.)
- Disaster Prevention Technology Research Center
Sinotech Engineering Consultants, Inc.
Basement No. 7 Lane 26, Yat-Sen Rd.
Taipei 11071, Taiwan R.O.C.
person@sinotech.org.tw
(P.-S.L.)